Geochemistry Geophysics Geosystems G3

AN ELECTRONIC JOURNAL OF THE EARTH SCIENCES

Published by AGU and the Geochemical Society

Article

Volume 9, Number 12

4 December 2008

Q12005, doi:10.1029/2008GC002100

ISSN: 1525-2027

Axial high topography and partial melt in the crust and mantle beneath the western Galápagos Spreading Center

Tanya M. Blacic

Department of Geology and Geophysics, University of Wyoming, Laramie, Wyoming 82071, USA (tblacic@uwyo.edu)

Garrett Ito

SOEST, University of Hawai'i at Manoa, Honolulu, Hawaii 96822, USA (gito@hawaii.edu)

Anjana K. Shah

U.S. Geological Survey, Box 25046, Denver, Colorado 80225, USA (ashah@usgs.gov)

Juan Pablo Canales and Jian Lin

Department of Geology and Geophysics, Woods Hole Oceanographic Institution, 266 Woods Hole Road, Woods Hole, Massachusetts 02543, USA (jpcanales@whoi.edu; jlin@whoi.edu)

[1] The hot spot-influenced western Galápagos Spreading Center (GSC) has an axial topographic high that reaches heights of ~700 m relative to seafloor depth ~25 km from the axis. We investigate the cause of the unusual size of the axial high using a model that determines the flexural response to loads resulting from the thermal and magmatic structure of the lithosphere. The thermal structure simulated is appropriate for large amounts of cooling by hydrothermal circulation, which tends to minimize the amount of partial melt needed to explain the axial topography. Nonetheless, results reveal that the large axial high near 92°W requires that either the crust below the magma lens contains >35% partial melt or that 20% melt is present in the lower crust and at least 3% in the mantle within a narrow column (<~10 km wide) extending to depths of 45–65 km. Because melt fractions >35% in the crust are considered unreasonable, it is likely that much of the axial high region of the GSC is underlain by a narrow region of partially molten mantle of widths approaching those imaged seismically beneath the East Pacific Rise. A narrow zone of mantle upwelling and melting, driven largely by melt buoyancy, is a plausible explanation.

Components: 12,278 words, 13 figures, 2 tables.

Keywords: axial high; Galapagos Spreading Center; partial melt; lithospheric flexure.

Index Terms: 3035 Marine Geology and Geophysics: Midocean ridge processes; 3045 Marine Geology and Geophysics: Seafloor morphology, geology, and geophysics; 8138 Tectonophysics: Lithospheric flexure.

Received 16 May 2008; **Revised** 31 August 2008; **Accepted** 3 October 2008; **Published** 4 December 2008.

Blacic, T. M., G. Ito, A. K. Shah, J. P. Canales, and J. Lin (2008), Axial high topography and partial melt in the crust and mantle beneath the western Galápagos Spreading Center, *Geochem. Geophys. Geosyst.*, *9*, Q12005, doi:10.1029/2008GC002100.

1. Introduction

[2] The topography of mid-ocean ridges displays a wide range of contrasting forms. Heavily faulted axial valleys >1 km deep occur along ridges with limited magma supply such as those with slow and ultraslow spreading rates. At the other end of the spectrum are axial topographic highs 20–50 km in width and rising 100–500 m above the surrounding topography. This morphology is associated with magmatically robust environments such as the fast spreading East Pacific Rise (EPR) [e.g., *Wang and Cochran*, 1993; *Scheirer et al.*, 1998]; portions of intermediate spreading centers such as the Valu Fa Ridge [*Collier and Sinha*, 1992], Juan de Fuca Ridge [*Hooft and Detrick*, 1995], Southeast Indian Ridge [*Sempéré et al.*, 1991], and Galápagos Spreading Center (GSC) [*Canales et al.*, 1997], as well as along the hot spot-influenced slow-spreading Reykjanes Ridge [*Searle and Laughton*, 1981]. Along the EPR, the axial topographic high is often accompanied by a positive free-air gravity anomaly (FAA) that is larger in amplitude than predicted if the high were isostatically supported by lateral density variations in the crust [*Wang and Cochran*, 1993; *Magde et al.*, 1995], an enigmatic finding that led to several hypotheses.

[3] In recent studies, researchers have proposed that the axial high topography and corresponding gravity signal reflect the thermal structure and stress state of mid-ocean ridge lithosphere and asthenosphere. One class of models, originally proposed by *Madsen et al.* [1984], suggests that the axial high results from an upward force exerted on the base of the lithosphere by buoyant, partially molten mantle. The combination of the strong positive free-air gravity signature and observed topography requires this low-density material to be narrow (~10 km) and extend deep (20–70 km) [*Wilson*, 1992; *Wang and Cochran*, 1993; *Magde et al.*, 1995]. As an alternative, *Eberle and Forsyth* [1998] suggested that dike injections above the magma lens relieve tension in the shallow crust and generate large vertical variations in horizontal stress. The resulting bending moment dynamically lifts the ridge axis and eliminates the need for a deep low-density mantle column. *Shah and Buck* [2001] have noted that all of these models require the lithosphere to cool and thicken slowly with age, whereas many studies based on seismic, compliance, and other data indicate that the lithosphere cools very rapidly with distance from the ridge [e.g., *Vera et al.*, 1990; *Toomey et al.*, 1994; *Crawford et al.*, 1999; *Cochran*, 1979; *McNutt*, 1979; *Phipps Morgan and Chen*, 1993; *Henstock et al.*, 1993; *Chen and Lin*, 2004; *Dunn et al.*, 2005]. *Shah and Buck* [2001] (see also *Buck* [2001] and *Shah and Buck* [2003]) showed that the axial high observed along the southern EPR can be explained by a narrow zone of partially molten crust that uplifts the axis combined with rapid near-axis melt solidification and strong crustal cooling by hydrothermal circulation, if topography on the flanks of the ridge is supported by flexure of the accreting lithosphere, and curvature at the ridge axis is allowed to form. The thermal/density structure of their model also satisfied the observed gravity anomaly without any additional buoyancy from melt in the mantle.

[4] Hot spot-related variations in thermal structure along the western Galápagos Spreading Center offer an opportunity to test the above-proposed causes of axial high topography. The western GSC spreads at an intermediate rate (full rate of 45–55 mm/a) and has an axial high that in many locations is appreciably larger in amplitude than most sections of fast spreading ridges such as the EPR. Moving westward from 91°W away from the Galápagos hot spot, the amplitude of the axial high decreases as crustal thickness decreases and as the depth of the axial magma lens increases [*Detrick et al.*, 2002; *Blacic et al.*, 2004] (Figure 1). This trend is the opposite of the trend that would be predicted by the model of *Eberle and Forsyth* [1998] (i.e., increasing the height of the dike zone above the magma lens would increase the hypothesized bending moments associated with extension), but it agrees with the general predictions of *Shah and Buck*'s [2001] model. Moreover, recent tomographic inversions of the wide-angle seismic data collected over the GSC show evidence for a narrow 8–15 km wide zone of partially molten crust with rapid cooling along its sides [*Canales et al.*, 2006]. Both sets of observations support the model of *Shah and Buck* [2001].

[5] In this study we use *Shah and Buck*'s [2001] model to investigate the density structure causing the cross-axis topography and gravity at two locations along the western GSC, one close to the influence of the hot spot where the axial high is large and one farther away from the hot spot where the axial high is smaller. Our data set consists of shipboard gravity and bathymetry combined with information about magma lens depth from multichannel seismic reflection observations and crustal thickness from seismic refraction data. The main

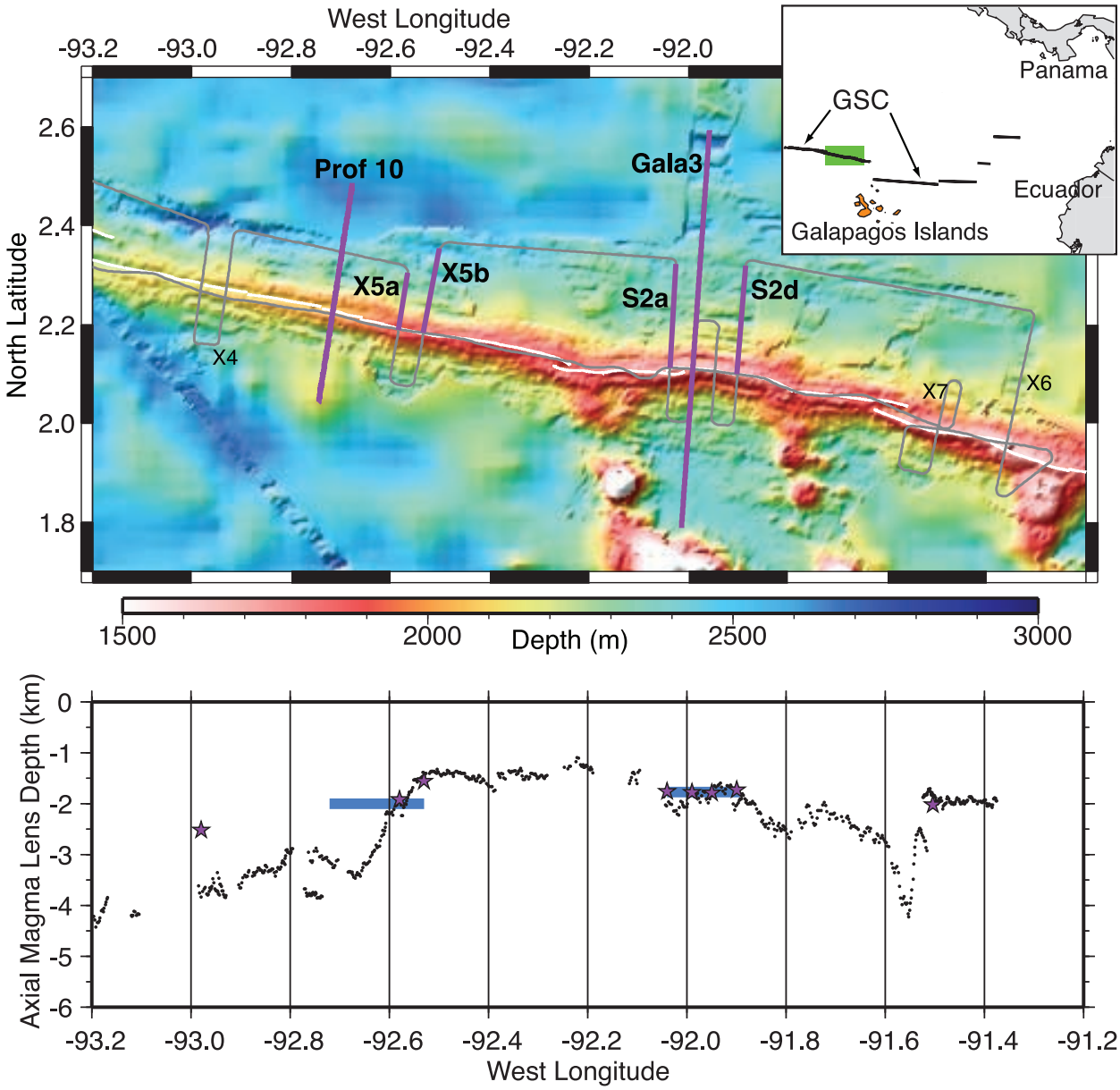

Figure 1. (top) Bathymetry map of the Eastern Province of the western Galápagos Spreading Center (GSC). Inset shows general location of the GSC and the study region (green box) in the eastern equatorial Pacific. Thick purple lines show the main cross-axis profiles used to create topography and gravity profiles for modeling. Grey lines mark the location of multichannel seismic (MCS) survey lines. White lines mark the ridge axis. (bottom) Depth below the seafloor to the top of the axial magma lens imaged in MCS lines. Stars are depth from cross-axis lines and black dots are depth from along-axis lines. Blue bars indicate average depths based on cross-axis multichannel seismic results. Average uncertainty in magma lens depth is ±110 m.

questions we address are (1) how much melt is present beneath these two hot spot-influenced regions of the GSC, (2) how deep does it extend into the crust and mantle in these regions, and (3) how important is melt in the crust versus the mantle in determining the amplitude of the axial high and how it changes along the western GSC? Following *Shah and Buck* [2001], we develop models of axial topography and gravity that include the effects of rapid off-axis cooling, melt solidification, and lithospheric flexure. The implied rates of hydrothermal cooling are near the upper range of what is expected at mid-ocean ridges and thus tend to minimize the amount of partial melt needed to explain the topography. In addition we explore a more complete set of solutions that allow

melt to extend into the mantle. We show that the ~400–700 m axial highs at the GSC are most likely associated with large fractions of partial melt both in the crust and extending substantially into the mantle below.

2. Data

[6] During the Galápagos Plume-Ridge Interaction Multidisciplinary Experiment (G-PRIME) in 2000 we collected multibeam bathymetry, gravity, seismic refraction, and seismic reflection data along the western GSC from ~91° to ~95.5°W. The GSC is ~200 km north of the Galápagos hot spot, thought to be centered beneath the western edge of the Galápagos Archipelago [*White et al.*, 1993]. Hot spot interaction with the GSC is expressed in a variety of forms including enhanced crustal thickness, elevated axial topography, changes in axial morphology, and changes in magma composition [e.g., *Detrick et al.*, 2002]. Influence in all of these measures along the western GSC is evident along the length of the ridge east of ~95.5°W to the large offset at ~91°W. Near the hot spot, between 91°W and ~92.5°W, the ridge axis is characterized by an axial high that is both taller and broader than that seen along the fast spreading EPR [*Canales et al.*, 1997; *Sinton et al.*, 2003]. The axial high disappears between ~92.5°W and the propagating rift tip at 93.25°W that marks the boundary of the Eastern Province of the ridge defined by *Sinton et al.* [2003]. West of 93.25°W, the ridge displays faulted, but flat (i.e., transitional) topography in the Middle Province before merging into ridge valley morphology west of 95.5°W in the Western Province. Seismic reflection and refraction data from the G-PRIME experiment (from axis-parallel lines located ~15 km off-axis) reveal a gradual decrease in near-axis crustal thickness away from the hot spot from 7.45 km at 92°W to 5.9 km at 94.25°W [*Canales et al.*, 2002]. Depth to the top of the axial magma lens is constrained by 13 axis-crossing seismic reflection lines from ~94.3°W to 91.5°W. The axial magma lens deepens gradually from a depth of ~1.5 km at 92.5°W to ~2.5 km at 93°W (Figure 1) corresponding with the decrease in the axial topographic high [*Blacic et al.*, 2004]. Note that differences in depth of the axial magma lens determined from cross-axis lines compared to along-axis lines in Figure 1 may be artifacts of the ship straying away from the ridge axis while shooting along-axis lines or could represent real changes in magma lens depth away from the axis [*Blacic et al.*, 2004]. For this reason, we use the cross-axis lines to define the shallowest magma lens depth at the axis in our areas of interest.

[7] We examine bathymetry and gravity data from two areas within the Eastern Province of the western GSC. The first area is centered at 92°W where the G-PRIME seismic refraction experiment Gala3 crosses the ridge axis. This area displays typical axial high morphology for the western GSC with a large topographic high ~675 m in amplitude and ~20 km in width [*Canales et al.*, 1997], the top of which is cut by a small axial trough less than half a kilometer wide and only tens of meters deep [*Blacic et al.*, 2004]. Crustal thickness in this area is well constrained to be 7.45 ± 0.25 km by the Gala3 seismic refraction data and *Canales et al.* [2002]. Axis-crossing seismic reflection data reveal an axial magma lens 1.7–1.8 km beneath the seafloor near 92°W [*Blacic et al.*, 2004]. Averaging the depths observed in four adjacent survey profiles (Figure 2), we obtain a representative depth of 1.75 km. This depth is near the maximum depths of magma lenses observed beneath the EPR (~1.65 km) [e.g., *Hooft et al.*, 1997; *Carbotte et al.*, 2000] despite the fact that the height and width of the Gala3 axial high is much larger than those observed at the EPR [e.g., *Scheirer and Macdonald*, 1993]. A simple calculation considering only Pratt isostasy shows that (for compensation depth equal to the base of the crust) if the axial high is to be supported by low-density melt only in the crust, it would require the volume below the melt lens to be nearly 100% melt. If we allow there to be 3% melt in the mantle down to a compensation depth of 50 km then ~51% melt is needed in the crust and for 5% melt in the mantle ~23% melt is needed in the crust. As we will show, the effects of off-axis cooling as well as lithosphere flexure to dynamically support the axial topography require less melt than the above values based on isostatic topography.

[8] At the second area, near 92.7°W, the axial high is significantly smaller (~475–500 m in height) and more similar to what is typically found along the EPR, although with a broader top and a more prominent axial summit trough than is typical at the EPR. Here we use data from the Gala96 Spanish cruise, which includes a bathymetry and gravity profile crossing the GSC at 92.7°W, hereafter referred to as Profile 10 after *Canales et al.* [1997] (Figures 1 and 2). GPRIME seismic data constrain the crustal thickness in this area to be ~6.75 km [*Canales et al.*, 2002] and both along- and across-axis seismic reflection profiles from

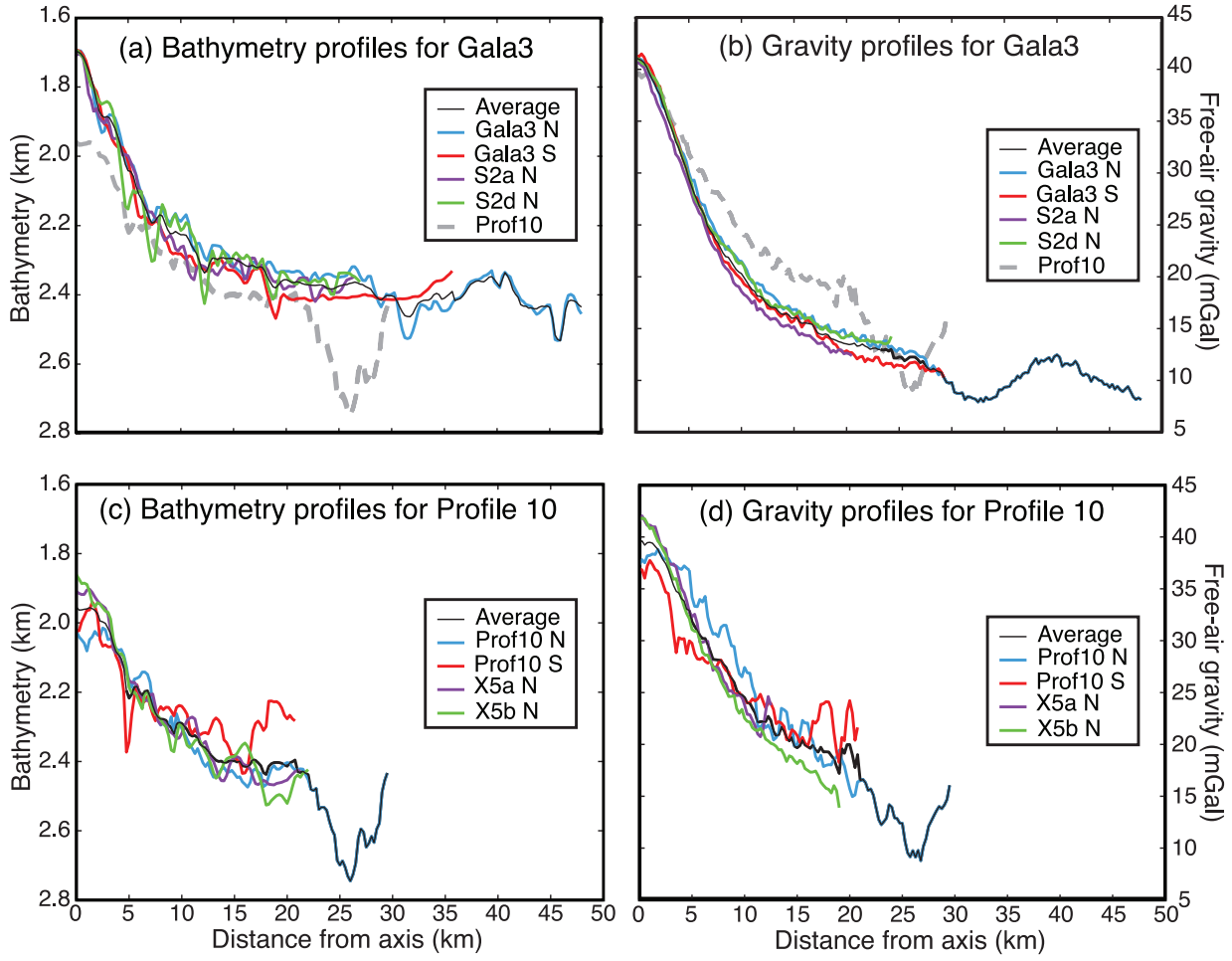

Figure 2. Data used to create observed average profiles to fit with models. (a) Topography and (b) free-air gravity profiles for the Gala3 area and (c) topography and (d) free-air gravity profiles for the Profile 10 area. Standard deviation difference between individual topography profiles and the average profile (black) is 34.4 m for Gala3 and 53.7 m for Profile 10. Standard deviation difference between individual gravity profiles and the average profile is 0.75 mGal for Gala3 and 2.0 mGal for Profile 10. These standard deviations are used as a measure of the uncertainty in our observed profiles. Average topography and gravity profiles for Profile 10 are plotted in Figures 2a and 2b (gray dashed line), respectively, for comparison with the Gala3 profiles.

92.58° to 92.98°W constrain the average magma lens depth to lie near 2 km (Figure 1). This depth is at least ~17% (~300 m) deeper than typical depths of the magma lens beneath the EPR [e.g., *Kent et al.*, 1993a, 1993b; *Detrick et al.*, 1993; *Hooft et al.*, 1997; *Tolstoy et al.*, 1997; *Carbotte et al.*, 2000]. Both the Gala3 and Profile 10 areas have significantly thicker crust than the 6 km assumed for the southern EPR by *Shah and Buck* [2001], allowing for the possibility of more partially molten lower crust than along the EPR. Meanwhile, the greater magma lens depth at the GSC reduces the required vertical extent of crustal melt in models.

[9] To best estimate average across-axis structure as well as its local variability, we examined several profiles with lengths adequately spanning the entire width of the axial high in each of the two areas. In the Gala3 area we compared the north and south sides of the Gala3 across-axis profile and the north sides of two nearby profiles (the south sides being too short to span the entire axial high): S2a, ~4.5 km to the west of Gala3, and S2d, ~11 km east of Gala3 (see Figure 1). Figures 2a and 2b show the topographic and gravity profiles, respectively, for each of these four lines. To produce the average topography profile (Figure 2a) we used bathymetry along these four profiles plus eight profiles extracted from the bathymetry swaths of these survey lines ~1.5 km to either side of the center beam. Thus, for each of the four main profiles two

additional bathymetry profiles were extracted from the swath data, one 1.5 km to the east and one 1.5 km to the west of the main profile. The standard deviation of the differences between these 12 individual profiles and the average profile is 34.4 m. To produce the average FAA we simply averaged the FAA along the four main profiles. Prior to averaging, however, we removed a long-wavelength regional trend evident by a ~8 mGal offset between points 29 km north and south of the axis along the Gala3 profile. This was done simply by subtracting the same north-south linear trend from Gala3 and the three adjacent profiles. The standard deviation of the differences between the four gravity profiles and the average profile is 0.75 mGal. We will use the standard deviation of the individual profiles with respect to the average profiles as a measure of the uncertainty of the observed across-axis variation of topography and gravity. This uncertainty will be used in assessing the range of acceptable models that successfully fit the average profiles.

[10] For the Profile 10 area we considered the north and south sides of Gala96 Profile 10 and the longer north sides of lines X5a (~14 km east of Profile 10) and X5b (~20 km east of Profile 10, see Figure 1). The bathymetry and gravity profiles for these four lines are shown in Figures 2c and 2d, respectively. For both topography and gravity, the average profiles were calculated from these four lines only (the Gala96 Profile 10 was not swath bathymetry). For the topography, the standard deviation of the differences between the individual profiles and the average profile is 53.7 m, and for the gravity it is 2.0 mGal.

3. Model Formulation

3.1. Governing Equations

[11] The model used in this study is based on that developed by *Shah and Buck* [2001] that calculates changes in gravity and topography resulting from variations in density with distance x from the axis. The model formulation is the same as that used in the work of *Shah and Buck* [2001]. Seafloor topography is calculated by solving the one-dimensional bending problem for a continually accreting lithospheric plate [*Kuo et al.*, 1986],

$$\frac{d(D\,d^3w/dx^3)}{dx} + \Delta\rho g w = q \tag{1}$$

where $w(x)$ is the downward deflection of the plate, $D(x)$ is the plate rigidity, $\Delta\rho$ is the density contrast between the mantle and water, g is the acceleration of gravity, and $q(x)$ is the applied vertical load distribution. Computationally, the above equation is treated by considering discretized changes in deflection $\Delta w(x)$ and subsurface loads $\Delta q(x)$ for a given distance of plate motion and accretion Δx:

$$\frac{d^2\Delta M_B}{dx^2} + \Delta\rho g \Delta w = \Delta q \tag{2}$$

where $\Delta M_B(x)$ is the incremental change in bending moment, related to Δw according to

$$\Delta M_B = D\frac{d^2\Delta w}{dx^2}. \tag{3}$$

Similar to *Shah and Buck* [2001], we assume that thin lithosphere and frequent magmatic activity allow the ridge axis to be in local isostatic equilibrium. The appropriate boundary conditions at $x = 0$ are $d^2\Delta w/dx^2 = d^3\Delta w/dx^3 = 0$ (or equivalently $d^3w/dx^3 = dw^4/dx^4 = 0$), and the conditions at $x = \infty$ are $w(0) = 0$ and $dw/dx = 0$. It should be noted that this formulation allows curvature to develop at the axis, which can significantly add to the dynamically supported axial high [*Buck*, 2001].

3.2. Thermal Structure, Subsurface Loads, and Flexural Rigidity

[12] The loads $q(x)$ and flexural rigidity $D(x)$ are ultimately derived from the thermal structure of the crust and mantle, which is imposed as illustrated in Figure 3. Model parameters are defined in Table 1. The depth to the 1200°C isotherm $H_{1200}(x)$ describes the rate of cooling of the plate, where 1200°C is the temperature at which melting starts. Near the axis, $H_{1200}(x)$ is set to the depth of the axial magma lens H_0 over a width W_0. For $x > W_0$, we simulate rapid cooling of the lithosphere by imposing $H_{1200}(x)$ to increase as a function of x^2 until at $x = W_1$ where it reaches a depth of H_1. Beyond this point, the isotherm deepens according to $H_{1200}(x) = H_1 + S(x - W_1)^{1/2}$, where the coefficient S controls the rate of deepening. The temperature increases linearly from 0°C at the seafloor to 1200°C at H_{1200}. Another option is to follow *Shah and Buck*'s [2001] assumption that the upper portion of the plate is efficiently cooled by hydrothermal circulation. We investigate this by setting temperature to increase linearly from 0°C to 400°C over the shallowest 75% of the depth to the 1200°C isotherm. In the lower 25%, we assume a linear increase in temperature from 400°C to 1200°C. We refer to this option as the case with depth-varying

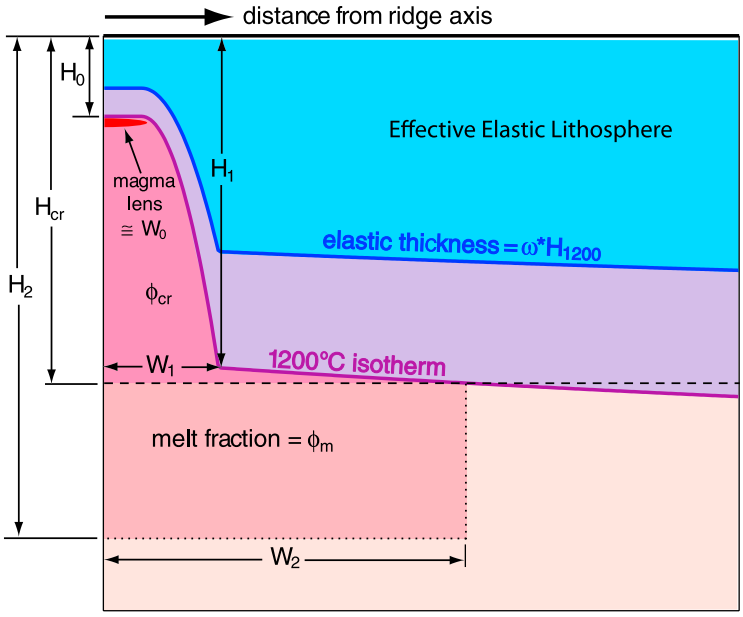

Figure 3. Schematic cartoon illustrating model set up and parameters. Partial melt is present below the 1200°C isotherm in the crust (dark pink region) and into the mantle (medium pink region) above a depth of H_2. See text and Table 1 for further description.

hydrothermal cooling. Partial melt is assumed to be present below the 1200°C isotherm and above the base of the crust until H_{1200} reaches the crustal thickness H_{cr}, which marks the horizontal extent of the melt region W_2.

[13] Three sources contribute to the loads $q(x)$ as the lithosphere evolves away from the ridge [*Shah and Buck*, 2001]: (1) thermal contraction of material due to cooling, $q_c(x)$, (2) solidification of partial melt, $q_{melt}(x)$, and (3) thermal bending stresses (TBS) resulting from material at varying depths cooling at different rates, $q_{tbs}(x)$. These three sources are summed to produce a total load $q(x)$

$$q(x) = q_c(x) + q_{melt}(x) + q_{tbs}(x). \tag{4}$$

The thermal contraction load q_c is determined by summing contributions from cooled material above the 1200°C isotherm:

$$q_c(x) = \int_0^{H_{1200}(x)} g\rho\alpha[T_{melt} - T(x,z)]\,dz \tag{5}$$

where ρ is the bulk density of the material at temperature T_{melt}, α is the volumetric coefficient of thermal expansion, and H_{1200} coincides with the top of the partially molten zone where $T = T_{melt} = 1200$°C.

[14] The load q_{melt} associated with partial melt consists of two terms

$$q_{melt}(x) = -\varphi_{cr}\Delta\rho_{cr}g[H_{cr}(x) - H_{1200}(x)] - \varphi_m\Delta\rho_m g[H_2 - H_{cr}(x)]. \tag{6}$$

The first term describes the contribution of partial melt in the crust where φ_{cr} is the average volume fraction of melt in the crust with a density contrast $\Delta\rho_{cr}$ relative to the surrounding rock at 1200°C in a column of height $H_{cr}(x) - H_{1200}(x)$. Expanding on the model of *Shah and Buck* [2001], we allow melt to extend further into the upper mantle and the effect of this additional hot molten material is included in the second load term. In this term the zone of partial melt has an average melt fraction of φ_m, density contrast of $\Delta\rho_m$, and melt column height of $H_2 - H_{cr}(x)$ for x less than W_2, where H_2 is the maximum depth over which appreciable partial melt is present. The width of the mantle melt column W_2 depends on the parameters that define the shape of the 1200°C isotherm in the crust (H_1, W_0, W_1, and S). For example, if H_1 is closer to the base of the crust, the 1200°C isotherm will cross into the mantle at a point closer to the axis than if H_1 is shallower. Although the melt fraction probably varies both vertically and horizontally within the melt zone, we consider a simplified situation in which φ_{cr} and φ_m represent average melt fractions within each partial melt zone in the crust and mantle, respectively.

Table 1. Symbol Table

Symbol	Parameter
	Material Properties
E	Young's modulus (9×10^{10} Pa)
g	Acceleration of gravity (9.81 m/s^2)
ν	Poissons ratio (0.25)
$\Delta\rho$	Density contrast between mantle and water (2300 kg/m^3)
$\Delta\rho_{cr}$	Density contrast between melt and crust rock (300 kg/m^3)
$\Delta\rho_m$	Density contrast between melt and mantle rock (600 kg/m^3)
α	Volumetric coefficient of thermal expansion (3×10^{-5} °C^{-1}).
T_{melt}	Melting temperature (1200°C)
	Variable Model Input Parameters
H_1	Depth to the 1200°C isotherm at the transition from rapid cooling to square root of distance cooling (m)
H_2	Depth to the base of the melt column (m)
W_0	Width of near-axis cooling (m, width of horizontal isotherms)
W_1	Width of rapid cooling zone (m, distance from the axis at which 1200°C isotherm reaches H_1)
W_2	Width of mantle melt column (m)
φ_{cr}	Average melt fraction in the crust
φ_m	Average melt fraction in the mantle
ω	Strength reduction factor
	Other Model Parameters
H_{cr}	Crustal thickness (m, from seismic data, *Canales et al.* [2002])
H_0	Depth to 1200°C isotherm near the axis (m, axial magma lens depth from seismic data, *Blacic et al.* [2004])
S	Coefficient of square root of distance cooling (m/m$^{1/2}$)
x	Horizontal distance from ridge axis (m)
$H(x)$	Depth to bottom of elastic plate (m, effective elastic plate thickness)
$H_{1200}(x)$	Depth to 1200°C isotherm (m)
$q(x)$	Total load distribution (Pa)
$q_c(x)$	Thermal contraction load (Pa)
$q_{melt}(x)$	Load from solidification of melt (Pa)
$q_{tbs}(x)$	Load from thermal bending stresses (Pa)
	Model Solution Variables
$w(x)$	Downward deflection (m)
$\Delta M_B(x)$	Incremental change in bending moment (N*m)
$D(x)$	Plate rigidity (N*m)

[15] The bending moments caused by thermal contraction stresses are implemented via a load term q_{tbs} based on the approach by *Parmentier and Haxby* [1986]. The method involves computing horizontal normal stresses due to thermal contraction as a function of depth and integrating these to find the associated moment and effective vertical load. This thin plate approximation tends to overestimate the deflection resulting from these stresses. Thus, we will examine results for cases both with and without TBS with the assumption that reality lies somewhere in between.

[16] The shallow thermal structure also controls how flexural rigidity $D(x)$ varies with distance in (1) and (2). Flexural rigidity depends on the effective elastic plate thickness $H(x)$ according to

$$D(x) = \frac{E[H(x)]^3}{12(1-\nu^2)} \tag{7}$$

where E is Young's modulus and ν is Poisson's ratio [e.g., *Turcotte and Schubert*, 1982]. Effective elastic plate thickness is assumed to be some fraction ω of the depth to the 1200°C isotherm, $H = \omega H_{1200}$ (Figure 3). The parameter ω takes into account the unquantified combined effects of faulting and the viscous-elastic-plastic behavior of the material above H_{1200} [*Shah and Buck*, 2001].

[17] With the net load $q(x)$ and rigidity $D(x)$ defined, we solve for seafloor topography by first solving equation (2) for incremental changes in plate deflection, using a fourth-order finite difference scheme. It is the lateral change in each of the above loads (Δq_c, Δq_{melt}, Δq_{tbs}, not the loads themselves) that sum to Δq in equation (2) and thus contribute to changes in plate deflection w with distance x. The total deflection $w(x)$ is then determined by integrating the incremental changes to each distance x.

3.3. Gravity Calculations

[18] The free-air gravity field is predicted by combining the effects arising from the modeled density structure of the lithosphere, the effects of seafloor topography, and corresponding relief on the crust-mantle boundary. Predicted gravity resulting from topographic variations of the seafloor and Moho are calculated using standard spectral techniques [*Parker*, 1973] in 2-D plan view assuming a uniform crustal thickness of 7 km and average crustal density of 2850 kg/m^3. The effects of crustal and mantle density variations are computed separately assuming 2-D structure in cross-section with a polygon formulation based on *Talwani et al.* [1959]. Density and topographic effects are then summed for comparison to observed free-air gravity profiles.

3.4. Model Misfits

[19] The misfit of each model profile is the root-mean squared (RMS) difference between the predicted and observed average profile. For the Gala3 location, RMS misfits are calculated from $x = 0$ to $x = 48$ km, but for the Profile 10 region, the misfits are calculated using only the first 22 km of the profiles due to the presence of a 300-m-deep trough ~22–29 km from the axis. Misfits that exceed the data uncertainty (as represented by the standard deviation of the individual profiles with respect to the average profile) are considered significant, whereas misfits less than or equal to the data uncertainty are indistinguishable and represent the best possible fits.

4. Results

4.1. Solving for Optimum Secondary Parameters

[20] Numerous variables control the details of the model subsurface. Crustal thickness and depth to the magma lens (H_{cr} and H_0) are constrained by seismic data and thus are taken as "known" quantities rather than parameters to solve. Similarly, the rate of slow (square root of distance) cooling outside of the near-axis zone, S, is also held fixed (for most cases) and assumed to be the same between the two regions based on bathymetric data. A value of $S = 45$ m/m$^{1/2}$ produces good fits to both locations on the GSC when depth variations in hydrothermal cooling are not included and is consistent with a half-space cooling model [*Turcotte and Schubert*, 1982] using a basal mantle temperature that agrees with results of *Parsons and Sclater* [1977]. We found that when depth variations in hydrothermal cooling are included, a lower value of S (30–36) was required to obtain good fits to the observed data, especially with TBS.

[21] The model parameters we solve are φ_{cr}, φ_m, H_2, H_1, W_0, W_1, and ω. Because we are interested in comparing melt quantity and location between our two profiles, we will consider the model parameters that most strongly influence the total amplitude of the bathymetry and gravity anomaly as the primary parameters: melt fraction in the crust φ_{cr} and in the mantle φ_m, and the depth to the base of the partial melt column H_2. These three primary parameters will be the focus of this study. The four secondary parameters (H_1, W_0, W_1, and ω), which define the details of the crustal thermal structure, most appreciably control the width of topographic high and the associated gravity signal but have a relatively minor effect on the total amplitudes of the bathymetry and gravity variations. Our modeling strategy is to first find sets of secondary parameter values (two sets for each profile, with and without TBS) that provide good fits to the observed gravity and bathymetry. We will then hold the secondary parameters constant while searching for the best fitting primary parameters.

[22] To identify the optimum values of the secondary parameters, we used an iterative process. Starting with the assumption that the melt fraction is the same throughout the entire melt region, i.e., $\varphi_{cr} = \varphi_m = \varphi$, we chose a pair of φ and H_2 values for which reasonable fits to the topography and gravity data could be obtained from a starting set of model parameters. We then varied H_1, W_0, W_1, and ω one at a time, while keeping the others constant, and chose the value at which a minimum RMS misfit for both topography and gravity was obtained. The cycle was repeated successively in order to converge on the most optimal set of values. Multichannel seismic images provided constraints on the

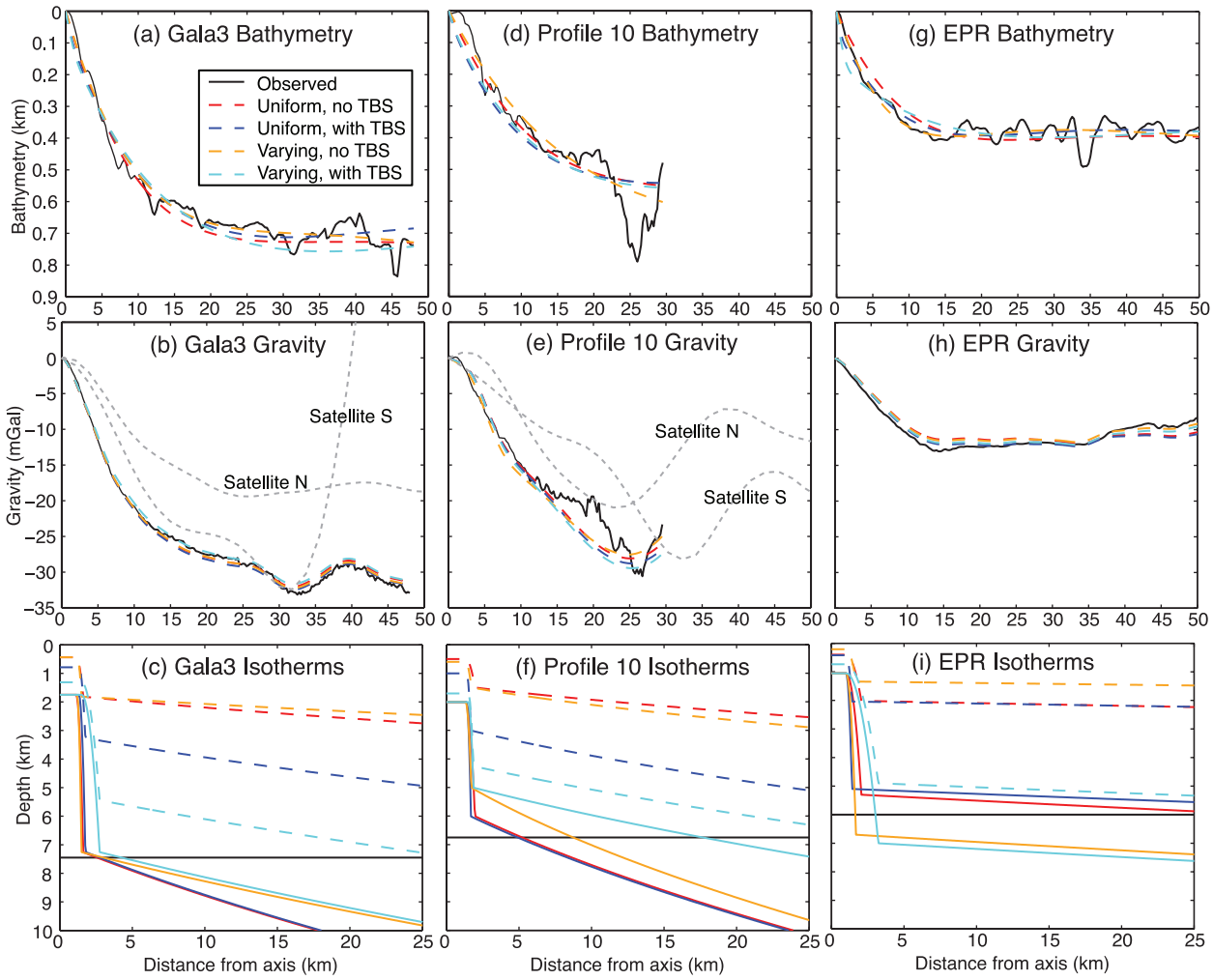

Figure 4. Sample model predictions for (a–c) Gala3, (d–f) Profile 10, and (g–i) the EPR. Figures 4a, 4d, and 4g show topography and Figures 4b, 4e, and 4h show FAA for the cases with and without thermal bending stresses (TBS) and with uniform or depth-varying cooling by hydrothermal circulation compared to the averaged observed profiles shown in Figure 2 for Gala3 and Profile 10. Average observed topography and gravity profiles for the EPR are from *Shah and Buck* [2001]. Profiles extracted from satellite gravity [*Sandwell and Smith*, 1997] for the north and south sides of the ridge axis are included for comparison (dashed gray lines in Figures 4b and 4e). Figures 4c, 4f, and 4i show the corresponding model geometry. Solid colored lines correspond to the 1200°C isotherm, dashed colored lines correspond to the effective base of the elastic crust, and solid black lines indicate the base of the crust. Table 2 shows model parameters and RMS misfit for topography (RMS_T) and gravity (RMS_G) for the model predictions in Figures 4a, 4b, 4d, 4e, 4g, and 4h. Values for H_1, W_0, W_1, S and ω in Table 2 are the optimum values hereafter.

half-width of the magma lens W_0 [*Blacic et al.*, 2004] allowing us to limit our search between 200 and 2000 m. Variations in the other parameters were limited to a reasonable range of values, beyond which misfits clearly increased: ~1000–5000 m for W_1, 0.0215–1.0 for ω, 1700–7600 m for H_1 at Gala3, and 2200–7300 m for H_1 at Profile 10. Separate sets of optimum parameters were determined for each of our two average profiles, for cases with and without TBS. Sample fits using our optimal parameter values are shown in Figure 4; parameter values used to obtain these fits are listed in Table 2. Model fits for the EPR are also shown in Figure 4 for comparison. For the EPR, we took one set of the averaged observed bathymetry and gravity profiles from one side of the axis used by *Shah and Buck* [2001] and found secondary parameters that gave the best fit with our model for their best values of φ and H_0 [see *Shah and Buck*, 2001, Figure 5]. The thermal structure in our model and thus model fits differ from those of *Shah and Buck*'s [2001] in some details, but the overall results are qualitatively the same.

Table 2. Model Parameters for Figure 4

	Gala 3 (Figures 4a–4c)				Profile 10 (Figures 4d–4f)				EPR (Figures 4g–4i)			
Parameter	Uniform, No TBS	Uniform With TBS	Varying, No TBS	Varying With TBS	Uniform, No TBS	Uniform With TBS	Varying, No TBS	Varying With TBS	Uniform, No TBS	Uniform With TBS	Varying, No TBS	Varying With TBS
H_0 (km)	1.75	1.75	1.75	1.75	2.01	2.01	2.01	2.01	1.05	1.05	1.05	1.05
H_{cr} (km)	7.45	7.45	7.45	7.45	6.75	6.75	6.75	6.75	6.0	6.0	6.0	6.0
H_1 (km)	7.25	7.25	7.25	7.25	6.0	6.0	5.0	5.0	5.3	5.1	6.7	7.0
H_2 (km)	30	30	30	15	30	20	20	10	6	6	6	6
W_0 (m)	1100	1300	1200	1500	1300	1400	1300	1500	1000	1000	1000	1000
W_1 (m)	1634	1798	1508	2888	2070	1763	1843	1987	2244	1497	1704	3225
W_2 (km)	2.5	2.7	3.0	4.3	5.7	5.4	8.8	17.6	–	–	–	–
φ	0.07	0.05	0.04	0.02	0.05	0.05	0.05	0.05	0.28	0.30	0.124	0.001
S	45	45	36	36	45	45	45	30	14	12	17	17
ω	0.25	0.45	0.25	0.75	0.25	0.5	0.3	0.85	0.38	0.4	0.2	0.7
RMS_T (m)	38	38	32	49	37	55	38	51	36	29	28	36
RMS_G (mGal)	0.6	0.6	0.5	0.8	2.2	2.5	2.4	2.9	1.0	0.8	0.8	0.6

[23] The width of the mantle melt column was not implemented as an independent model parameter. However, we can test the effect of increasing W_2 on the predicted model fits (Figure 5). Gala3 appears to require a narrow melt column in the mantle with misfits for both topography and gravity increasing rapidly with increasing W_2. In contrast, Profile 10 shows differing sensitivity for topography and gravity misfits with topography misfit increasing while gravity misfit decreases with increasing W_2. The magnitude of the changes in misfits for Profile 10 is small, however, implying that we cannot distinguish between fits in the range of W_2 shown in Figure 5 at Profile 10 (though a slightly greater W_2 may provide a better fit to the width of the axial high and gravity anomaly). Note that our optimum values of H_1 are near H_{cr} and are the same for cases with and without TBS. Of the four secondary parameters, H_1 most influences the height of the topography and magnitude of gravity anomalies because it determines the height of the narrow melt

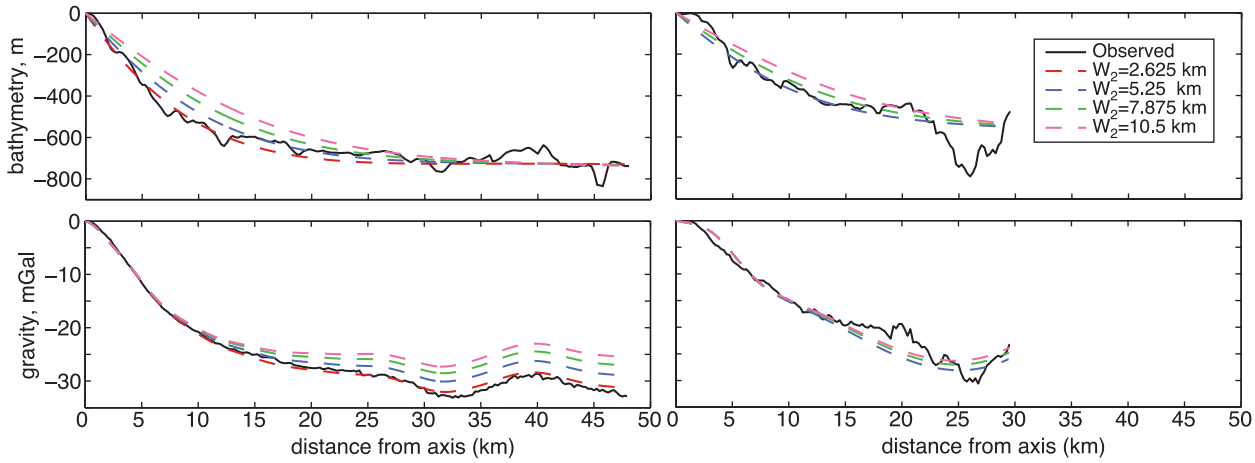

Gala3

W_2	RMS_T	RMS_G
2.625 km	1.10	0.85
5.25 km	1.22	2.61
7.875 km	1.77	4.27
10.5 km	2.44	5.60

Profile 10

W_2	RMS_T	RMS_G
5.25 km	0.69	1.13
7.875 km	0.66	0.93
10.5 km	1.03	0.81

Figure 5. Sample model fits for increasing width of mantle melt column, W_2. Tables show normalized RMS misfits for topography (RMS_T) and gravity (RMS_G) profiles.

column in the crust as well as the size of the wedge-shaped region of partial melt in the lower crust (Figure 3). Thus, to more directly compare cases with and without TBS, for all cases H_1 is set to the optimum value for the case without TBS. Doing so yields slightly higher misfits for cases with TBS for Profile 10 but not for Gala3 (e.g., Figure 4). Results from a study of the Oman ophiolite suggest that the top 50% of the gabbro layer cooled much faster than the bottom [*Garrido et al.*, 2001]. This implies that H_1 should be approximately $(H_{cr} + H_0)/2$; however, this value of H_1 results in a large wedge-shaped melt region in the lower crust of our models and thus fails to produce good fits to the width of the axial high for most cases.

[24] The large optimum values of H_1 simulate dramatic crustal cooling due to hydrothermal circulation. For comparison with prior studies we can estimate the effective Nusselt number, *Nu* (the ratio of hydrothermal heat transport within a permeable layer to heat transport by heat conduction alone), which is simulated by determining what value of thermal diffusivity results in the isotherm depths of our model at a distance x equal to the width, W_1, of the zone of rapid crustal cooling. Using a standard equation for the cooling of a semi-infinite half-space [e.g., *Turcotte and Schubert*, 1982], we find that for Gala3 with uniform hydrothermal cooling and without TBS, *Nu* = 9.9 for the 600°C isotherm (above which hydrothermal circulation is thought to be occurring, e.g., *Phipps Morgan and Chen* [1993]). Including depth-varying hydrothermal cooling increases *Nu* to 28.3. When we attempt to keep partial melt entirely within the crust with a melt fraction of 20% (uniform hydothermal cooling and no TBS), our parameter H_1 must be increased to depths greater than 20 km, generating an unreasonably large *Nu* of ~83 (or ~70 with depth-varying cooling) for the same isotherm. Our optimal secondary parameter values keep H_1 within the crust so that *Nu* is within reasonable ranges when hydrothermal cooling is uniform with depth. It is primarily for this reason that we focus on models without depth-varying hydrothermal cooling for both Profile 10 and Gala3 below. This parameter choice works to maximize the effects of thermal densification and minimize the effects of partial melt on our predicted surface anomalies. A lower amount of thermal densification (using a shallower value of H_1) would require a higher mantle melt fraction than our conservative estimates, but would also effectively reduce *Nu* further. Nonetheless, for our secondary parameter choices, thermal densification contributes a smaller amount to the model topography (~35% for Gala3 without TBS) compared to the solidification of partial melt (remaining ~65%). In summary, the thermal structure simulated represents an off-axis rate of cooling that is at the upper range of previous estimates and thus leads to conservative predictions as to the amount and height of the melt column required to fit the observed topography and gravity.

4.2. Results for Profile 10

[25] Sample fits to Profile 10, located farther from the hot spot are shown in Figure 4 for the case with a single melt fraction φ for the entire melt region. When TBS are not included, a relatively low flexural rigidity (i.e., similar thermal structure but lower ω) is required compared to the case with TBS. The width of the crustal melt column is nearly the same for both cases.

[26] Using the optimal values of the secondary parameters (for cases with and without TBS, uniform hydrothermal cooling) (Table 2), we now vary melt fraction $\varphi(= \varphi_{cr} = \varphi_m)$ and melt column height H_2. Contour plots of RMS misfit, normalized by observational uncertainty (Figure 2), are plotted in Figure 6. The contour lines enclose a narrow region or "trough" of minimum RMS. For topography, the shape of this trough of minimum misfit displays an approximately inverse relationship between melt fraction φ and vertical extent of melt H_2. This behavior can be simply explained by the consideration that the total melt buoyancy force is the product of φ and H_2. For gravity, the trough of minimum misfit qualitatively follows a similar form but levels off near $\varphi \sim 0.1$ and for $H_2 \geq \sim 40$ km; such behavior is not surprising given the decrease of surface gravity signal with the inverse square of source distance. In contrast to prior studies of the EPR [*Wang and Cochran*, 1993; *Magde et al.*, 1995], both topography and gravity allow for substantial melt to be present in the mantle as well as in the crust beneath the GSC, with equal misfits over a large range of depths.

[27] To better constrain values of φ and H_2 that produce the best fits for both the topography and gravity, we averaged together normalized misfits for topography and gravity to produce contour plots of misfit that take into account both gravity and topography constraints (Figures 6c and 6d). Cases with and without TBS yield similar solutions for φ and H_2 (but again with different secondary parameters, Table 2). Models that assume all melt is contained within the crust (H_2 equal to the

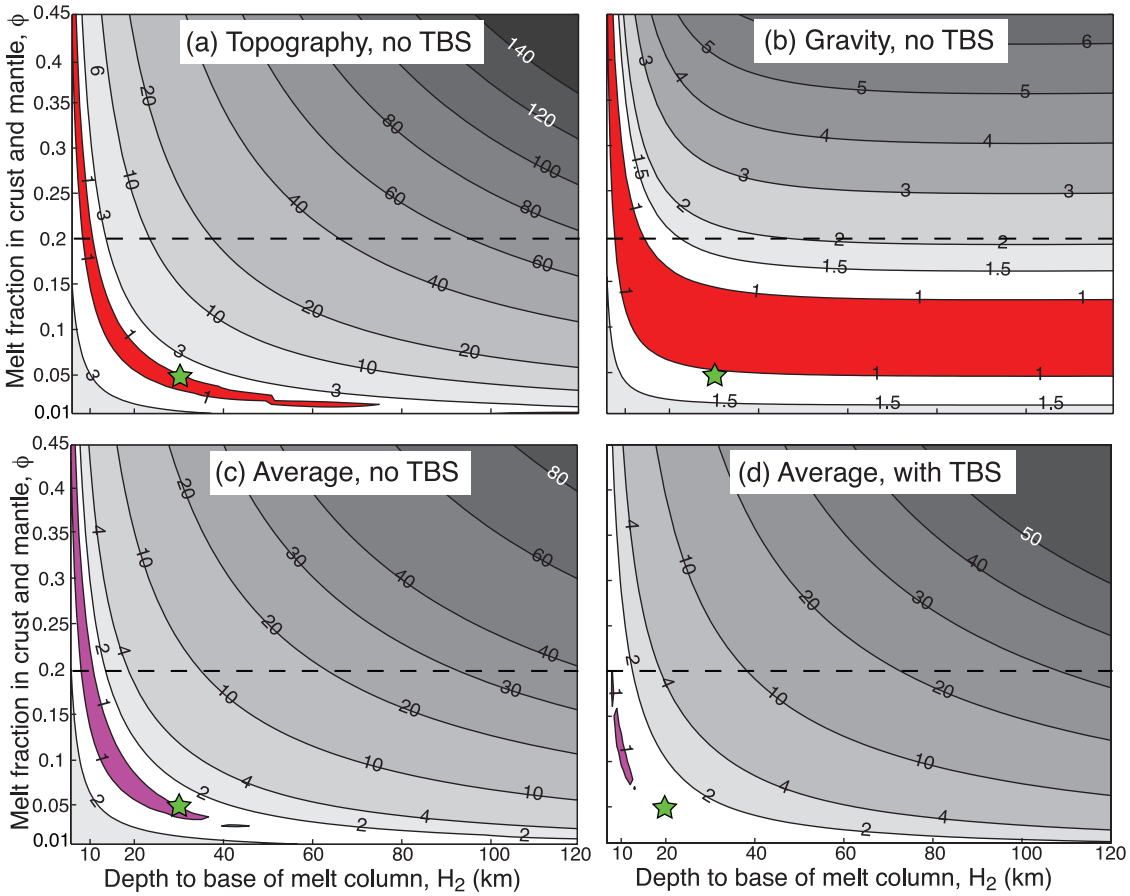

Figure 6. Contour plots of RMS misfit for model predictions for Profile 10 with $\varphi_{cr} = \varphi_m = \varphi$ for variations in melt fraction φ of 0.01–0.45 and depth to the base of the melt column H_2 of 6.75–120 km. Other model parameters are as shown in Table 2. Misfit is normalized by the data uncertainty (i.e., standard deviation of the variation of individual profiles relative to the averaged profile). Colored regions highlight model solutions with normalized RMS misfit of 1.0 or less. Green stars show the location of the model fits from Table 2. Dashed line marks reference upper-bound for the mean melt fraction in mid-ocean ridge crust based on tomography and seafloor compliance studies at the EPR [*Crawford et al.*, 1999; *Dunn et al.*, 2000]. (a) Normalized RMS misfit for topography model predictions for the case without TBS. (b) Normalized RMS misfit for predicted gravity for models without TBS. Normalized misfits for topography (Figure 6a) and gravity (Figure 6b) are averaged to produce average misfits for models (c) without and (d) with TBS. Figures 6c and 6d thus show the region of best fit using constraints from both gravity and topography.

crustal thickness or all cases along the vertical axis in Figure 6) require a large melt fraction to fit both the gravity and topography: $\varphi \geq 0.35$ for models both with and without TBS. For reference, a seismic tomography study indicates that the lower crust of the EPR contains $\leq \sim$20% melt on average [*Dunn et al.*, 2000] (dashed line in Figure 6). Thus, where the axial high along the GSC is comparable in height to that along the EPR, either there is a lot more melt in the GSC crust or the melt column in the GSC upper mantle is partially supporting the axial topographic high.

[28] This result contrasts with that of *Shah and Buck* [2001], who showed that the cross-axis EPR gravity and topography could be explained with melt contained entirely in the crust with reasonable crustal melt fractions. Indeed, we successfully reproduced their results for the EPR with similar secondary parameter values for the same φ as *Shah and Buck* [2001] (Figure 4). However, we could not fit the GSC Profile 10 observations with melt fractions lower than 35%, present only in the crust. Key factors are that, compared to the typical EPR, while the Profile 10 axial high is of comparable magnitude, the axial high is wider by $\sim$10 km, the magma lens is approximately twice as deep, and the positive free-air gravity anomaly is nearly twice as large. When the gravity anomaly is corrected for the effects of topography at the water/crust

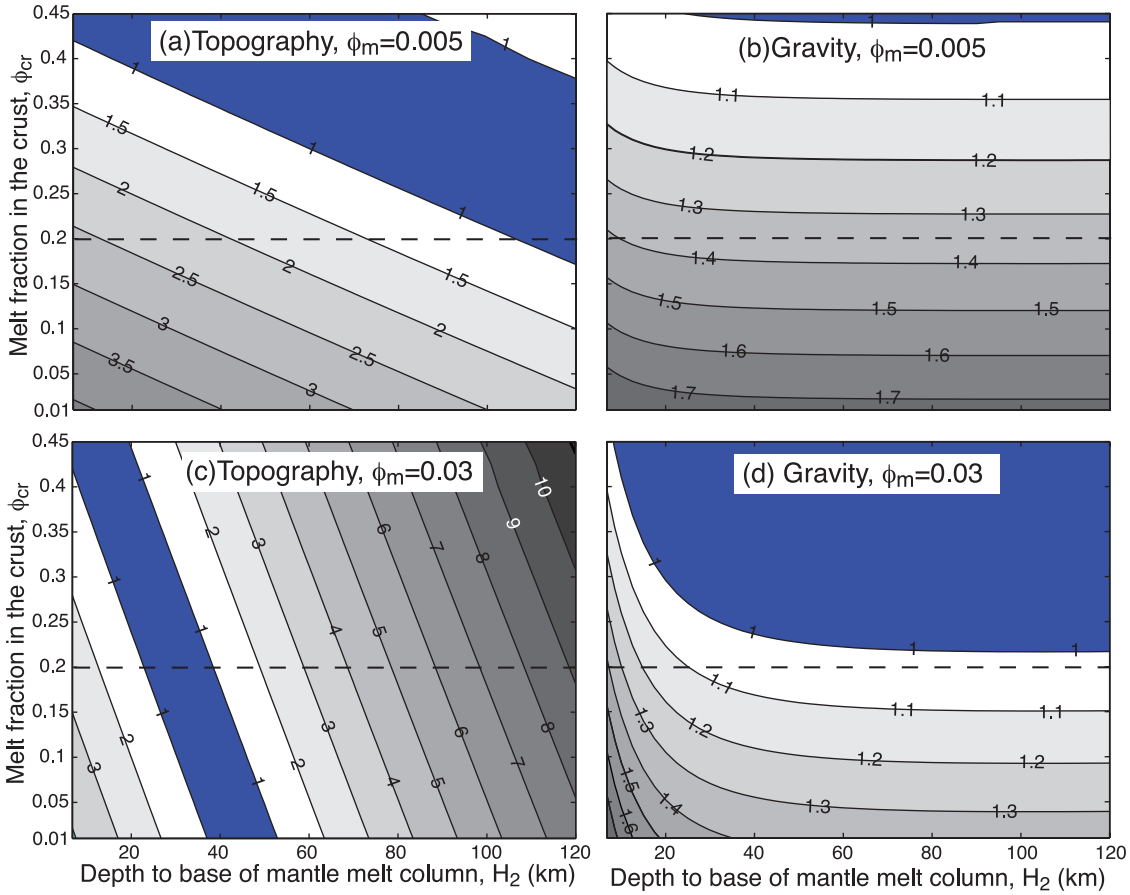

Figure 7. Contour plots of normalized RMS misfit to Profile 10 for models with mantle melt fraction φ_m set independent of the crustal melt fraction φ_{cr} and no TBS. Fraction of melt in the crust φ_{cr} increases along the vertical axis while the depth of partially molten mantle (H_2 from 6.75 to 120 km as in Figure 6) increases along the horizontal axis. Other parameters are as listed in Table 2. Colored regions highlight model solutions with normalized RMS misfit of 1.0 or less. Dashed line marks reference maximum crustal melt fraction as in Figure 6. Normalized misfit for topography predictions with (a) φ_m = 0.005 and (c) φ_m = 0.03. Normalized misfit for gravity predictions with (b) φ_m = 0.005 and (d) φ_m = 0.03.

and crust/mantle interfaces assuming crust of constant thickness, the cross-axis anomaly relief is ~13 mgal, which is ~30–160% greater than observed along the EPR [e.g., *Madsen et al.*, 1990; *Wang and Cochran*, 1993; *Magde et al.*, 1995; *Shah and Buck*, 2006].

[29] Assuming uniform melt fraction in the crust and mantle is probably a poor representation of the natural structure. Seismic refraction studies of the EPR show that there is likely to be much more melt per unit volume in the crust than in the mantle [e.g., *Dunn et al.*, 2000]. We therefore explore a set of models with crustal melt fractions φ_{cr} = 0.01–0.45 and for mantle melt fractions of φ_m = 0.005, 0.01, 0.03, and 0.05. Contour plots of normalized RMS misfit in Figure 7 show the effects of increasing the amount of melt in the crust on the vertical axis (increasing φ_{cr}) and increasing the depth H_2 of partially molten mantle on the horizontal axis. Each plot shows results for a fixed mantle melt fraction φ_m, without TBS. For very little melt in the mantle (φ_m = 0.5% Figure 7a) best fits to topography require at least 20% melt in the crust and a mantle melt column that could extend up to more than 100 km deep. The gravity, however, does not fit well with this model of little melt in the mantle. Increasing φ_m to 0.03 significantly affects the fit to the topography (Figure 7c). For φ_{cr} near the reference maximum of 0.2, models only need a mantle melt region with 3% melt extending to a depth of ~30 km. For smaller φ_{cr}, the mantle melt region can extend as deep as ~55 km. The gravity modeling, however, still requires high φ_{cr} for φ_m = 0.03 (Figure 7d).

[30] Figure 8 shows contours of normalized RMS misfit for gravity and topography averaged together

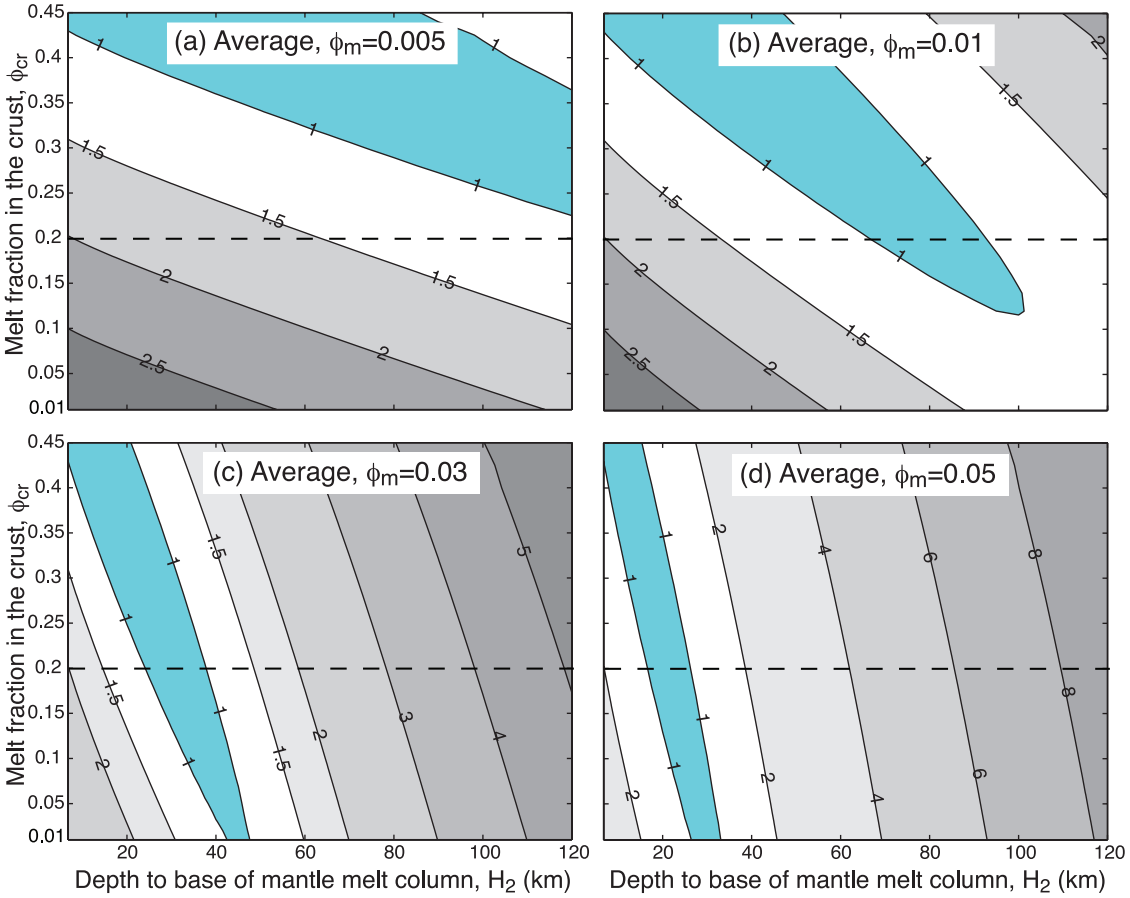

Figure 8. Normalized misfits for two-porosity models of Profile 10 topography and gravity in Figure 7 (no TBS) are averaged together for each value of φ_m to show regions of best fit using constraints from both observed topography and gravity. Axes and dashed lines are the same as in Figure 6. Colored regions highlight model solutions with normalized RMS misfit of 1.0 or less. (a) φ_m = 0.005, (b) φ_m = 0.01, (c) φ_m = 0.03, (d) φ_m = 0.05.

for four values of φ_m. Best fitting solutions with $\varphi_{cr} \leq 20\%$ and $\varphi_m = 1\%$ require a very tall mantle melt column, extending to ~60–100 km depth. For φ_m = 3–5%, we can have φ_{cr} = 20% with the mantle melt column extending to 20–40 km depth and φ_{cr} as little as 1% with $H_2 \sim$ 30–50 km. Including TBS decreases the range of H_2 and φ_{cr} required for the best fits. For example when φ_m = 3%, H_2 could extend from ~10 to 25 km depth with $2\% \leq \varphi_{cr} \leq 20\%$.

4.3. Results for Gala3

[31] The Gala3 profile represents the region along the GSC most influenced by the Galápagos hot spot and exhibits the largest axial topographic high. At this location, the crust is thicker (~7.5 km) and the magma lens is shallower (~1.75 km) compared to Profile 10. Figure 4 shows sample fits for Gala3 for a single melt fraction φ for the entire melt region. Much like Profile 10, when thermal bending stresses are included, larger flexural rigidities and slightly less melt are required to obtain an axial high of the same amplitude. Gala3 also requires a slightly narrower, lower crustal melt zone compared to Profile 10. In detail, the differences in thermal structure between Profile 10 and Gala3 imply different cooling rates, heating rates by magma transport, or both, but these differences are controlled by our secondary parameters which were not the emphasis of our study and therefore it would be inappropriate to speculate about the geologic causes of such details. The most robust characteristics of both profiles are dramatic thickening of the lithosphere over a short distance from the axis, which leads to a narrow melt column in the crust ≤4 km and in the mantle ≤~10 km (total widths).

[32] Contour plots of normalized RMS misfit are shown in Figure 9 for a single melt fraction φ in the crust and mantle. As for Profile 10, the trough of

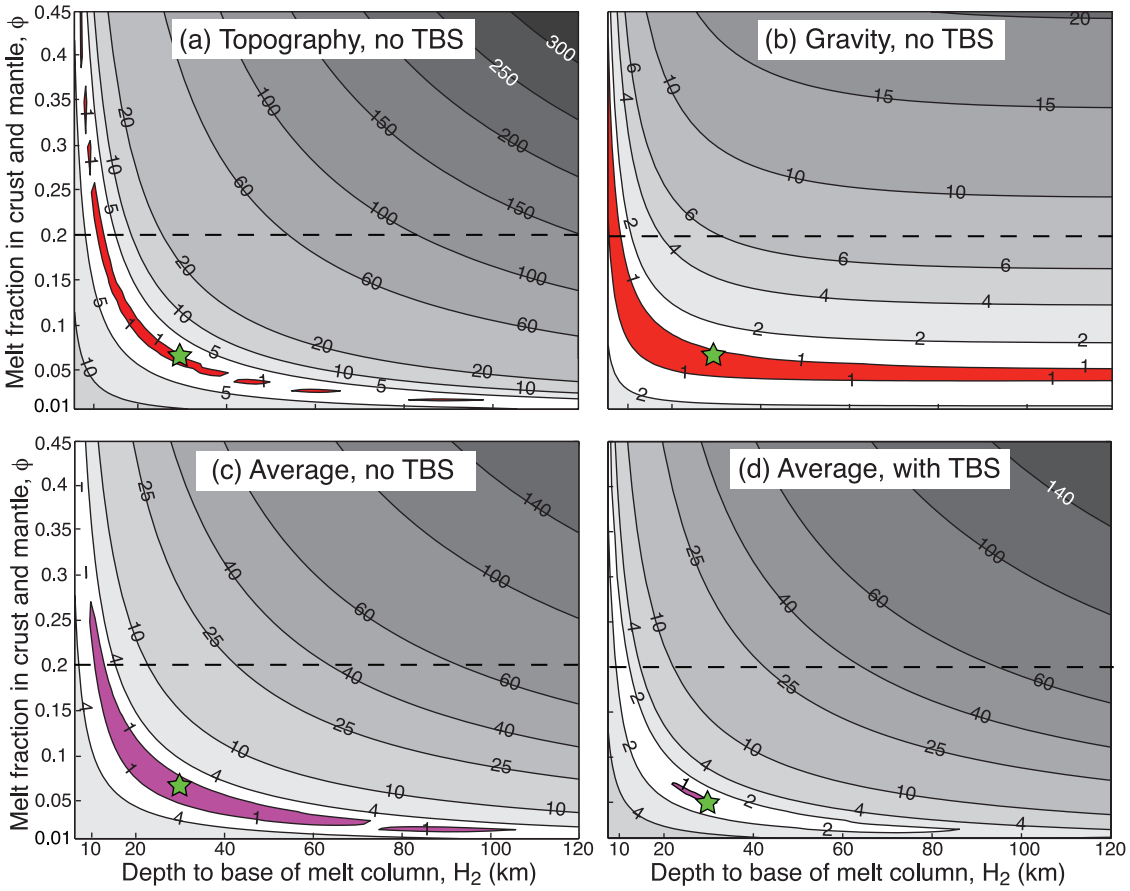

Figure 9. Same as Figure 6 but for Gala3, except the minimum depth shown is the crustal thickness of 7.5 km.

minimum misfit shows an approximately inverse relation between φ and melt column height H_2 for topography; the gravity model shows a similar form but the fit levels off near minimum melt fraction of $\varphi \sim 0.06$ (which is lower than for Profile 10) for $H_2 \geq \sim$40 km. Normalized RMS misfits averaged between topography and gravity models for cases with and without TBS are shown in Figures 9d and 9c, respectively. The troughs of minimum misfit extend to greater melt depths and only slightly lower melt fractions compared to those for Profile 10 (Figure 6).

[33] When the melt fraction in the mantle is allowed to differ from the melt fraction in the crust we obtain results as shown in Figure 10. For mantle melt fraction of 0.005 (Figures 10a and 10b) the topography requires too much melt in the crust and a deep mantle melt column to reach a minimum RMS misfit, while the gravity can be fit with φ_{cr} near 20% and H_2 as shallow as ~30 km. With a larger mantle melt fraction (φ_m = 0.03, Figures 10c and 10d), the topography can be fit with φ_{cr} < 20% and H_2 ~50–65 km. The gravity can be fit with a very shallow mantle melt column with φ_{cr} close to 20%. Contour plots of averaged topography and gravity misfits (Figure 11) show that models need at least 3% melt in the mantle melt column to adequately fit both the gravity and the topography while keeping φ_{cr} below 20%. For a mantle melt column containing 3% melt, models best fit the observations for $0.08 \leq \varphi_{cr} \leq 0.2$ if the melt column extends ~45–60 km deep. For φ_m = 0.05, φ_{cr} can be 0.01–0.2 with H_2 between ~35 and 40 km. Including TBS reduces the H_2 and φ_{cr} needed to fit both the topography and gravity for each value of φ_m we investigated. For example, for φ_m = 0.03 models best fit the observations with H_2 between ~35–45 km for $0.08 \leq \varphi_{cr} \leq 0.2$. Compared to Profile 10, the Gala3 area appears to require higher φ_m and/or H_2 (Figures 8 and 11).

4.4. Effects of Magma Lens Depth and Crustal Thickness

[34] Since a large contribution to both topography and gravity variations comes from the high melt fractions in the lower crust, it is prudent to examine

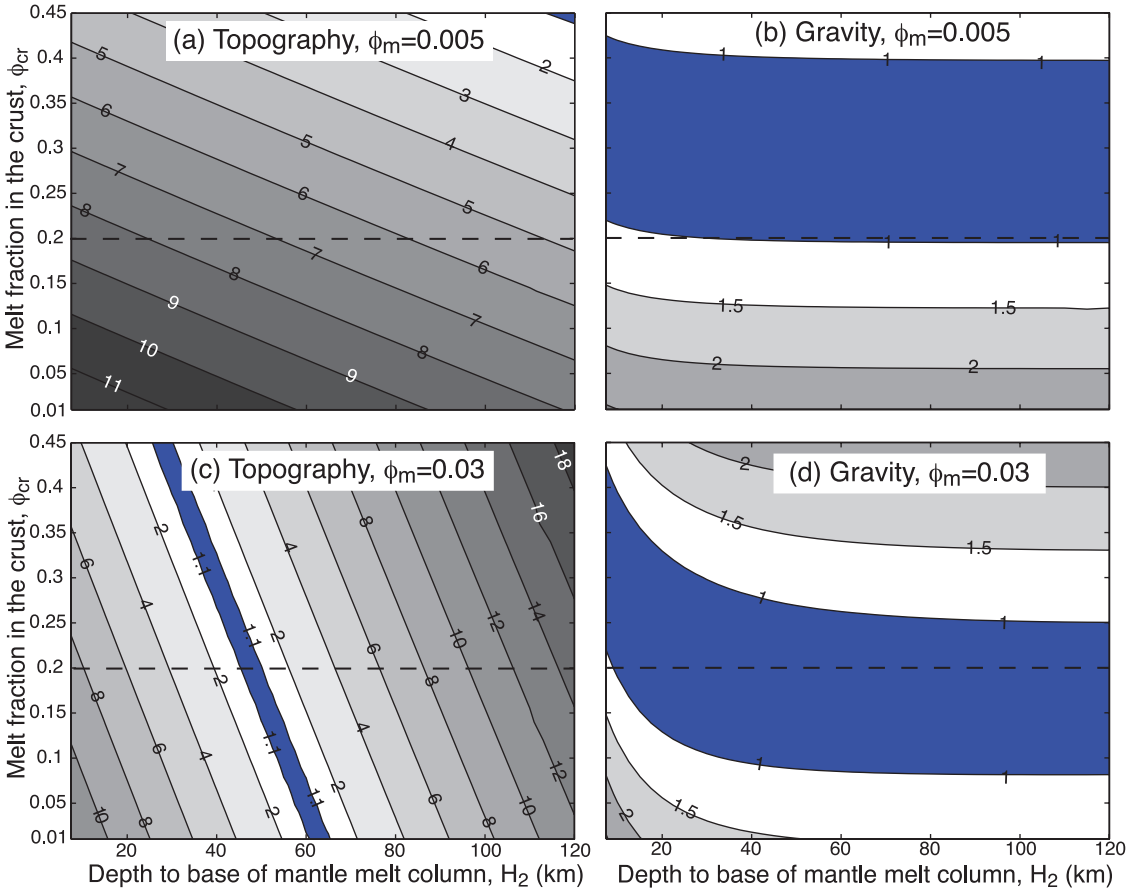

Figure 10. Same as Figure 7 but for Gala3 and the horizontal axis starting at the crustal thickness of 7.5 km.

to what extent the along-axis variations in the total height of the crustal magma zone affect the surface structure. The total height is the difference between two seismically imaged boundaries: the base of the crust and the magma lens (i.e., $H_{cr} - H_0$). Figure 12 shows how the observed axial topography varies as a function of $H_{cr} - H_0$, which generally increases west-to-east along this portion of the GSC. It is interesting to note, however, that the section of the EPR used by *Shah and Buck* [2001] in their study falls in the middle of the trend of the observations from the GSC, implying that the relationship may be more than a local phenomenon. For comparison we show two curves in which $H_{cr} - H_0$ is varied by changing H_0 while the optimum secondary parameter values from Table 2 (uniform hydrothermal cooling and no TBS) are held fixed for each of Profile 10 and Gala3. It is clear that the seismically constrained variations in ($H_{cr} - H_0$) alone contribute only a fraction to the observed changes in the axial topography even when variations in the near-axis elastic plate thickness (i.e., due to variations in H_0) are included in our calculations. The finding that the axial height decreases more rapidly with $H_{cr} - H_0$ then the model curves in Figure 12 predict indicates that factors in addition to $H_{cr} - H_0$, which also vary with $H_{cr} - H_0$, must contribute to topography. For lower axial highs, especially those with normal faults, a combination of nonisostatic tension [e.g., *Chen and Morgan*, 1990; *Shah and Buck*, 2003] and reduced construction of topography by magmatism [*Ito and Behn*, 2008] could be factors that correlate with $H_{cr} - H_0$ and further reduce topography. The latter mechanism is supported by model predictions that explain a global positive correlation of axial depth (from axial highs with deep valleys) with H_0 by *Ito and Behn* [2008]. Our model results suggest another possibility, which is that the amount of partial melt in the crust and mantle changes along the ridge axis.

5. Discussion

[35] Our results for both profiles (Figure 13) indicate that, in addition to a melt-rich lower crust, the GSC also has an appreciable fraction of melt

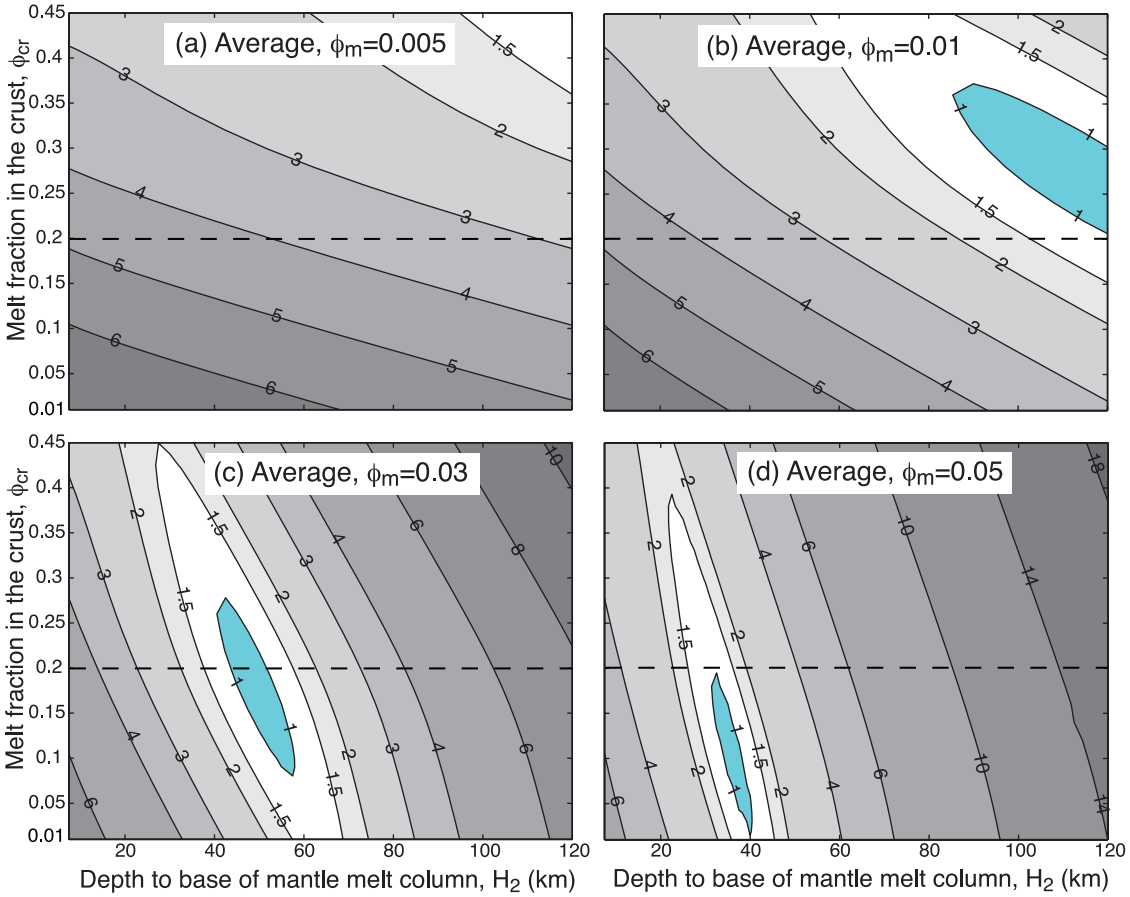

Figure 11. Same as Figure 8 but for Gala3 and axes the same as Figure 10.

extending into the mantle. The possibility of more melt beneath Gala3 (i.e., greater φ_{cr}, φ_m, and/or H_2) than beneath Profile 10 is apparent for the solutions both with and without TBS, although when TBS are included the amount of melt needed is less for both regions. In all cases, both regions of the GSC require a lot of partial melt in the lower crust ($\geq$20%) and/or upper mantle ($\geq\sim$3%) to support the axial high topography.

[36] One simplifying assumption of our models is that the plate is effectively "broken" at the axis by frequent diking such that it supports no shear stress and reaches an isostatic height. Near Gala3, where the axial magma lens is shallow, this approximation is likely to be more appropriate. However, as the axial lithosphere thickens, as it does around Profile 10, nonisostatic stresses at the axis could start to develop. Nonisostatic stresses would tend to reduce the height of the axis and increase the width of the high, which implies that our models could actually underestimate the amount of melt (φ_{cr}, φ_m and/or H_2) beneath the GSC and overestimate the width of the crustal melt column. This could help to explain why at Profile 10 it appears that more melt is needed to model the observed gravity than is needed to model the observed topography (Figure 7). In this case, the gravity may be a more accurate reflection of the amount of melt present in the lower crust and upper mantle, and the difference in the amount of melt beneath Profile 10 and Gala3 may be smaller than our results currently suggest.

[37] Both the large axial high and narrow melt column at the GSC are likely to be related to the Galapagos hot spot. The hot spot influence is largest near Gala3 and is less near Profile 10 [*Detrick et al.*, 2002] as seen by thicker crust and less dense mantle, which together support the along-axis swell [*Canales et al.*, 2002]. The large volume of melt needed beneath Gala3 by our models is fully consistent with the evidence for lower mantle densities inferred by *Canales et al.* [2002] from along axis variations in long wavelength topography and gravity. Geochemical anomalies are also larger near Gala3 compared to Profile 10 [*Cushman et al.*, 2004]. In fact, the

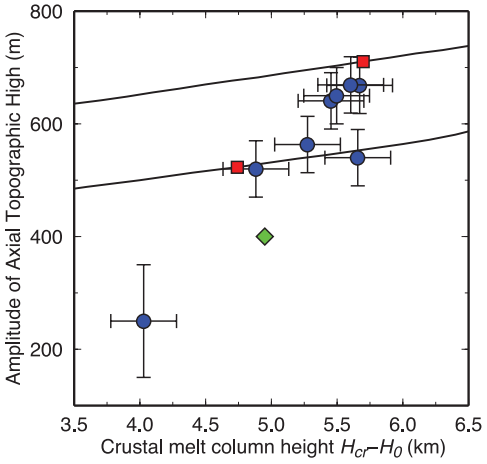

Figure 12. Effect of varying the total lower crustal melt column height $H_{cr} - H_0$ on the amplitude of the axial topographic high. Blue circles are observed values from GPRIME bathymetry and seismic data (stars in Figure 1). Red squares are model results for Gala3 and Profile 10 shown in Figure 4 for the case with no TBS and uniform hydrothermal cooling. Lines show model predictions for each profile, without TBS, in which $H_{cr} - H_0$ is varied by changing H_0 while other model parameters are held at their optimum values as defined in Table 2. Green diamond is for the EPR 8°–8°15′S from *Shah and Buck* [2001].

evidence for more water in the mantle beneath Gala3 suggests a taller melt column in the area due to the reduction in mantle solidus temperature. A taller melting column is consistent with the possibility of Gala3 having a taller column of high melt fraction that supports the tall axial high topography.

[38] Seismic studies are also consistent with our model results. As mentioned in the Introduction, a narrow partially molten lower crust is evident in tomographic inversions from the GPRIME wide-angle seismic data [*Canales et al.*, 2006]. The narrow cross-axis widths simulated here (~2.5–4 km total width) are consistent with the 8 km width estimated by *Canales et al.* [2006], when considering the tendency for tomographic methods to smear localized features over broader areas. The need for high melt fractions in the GSC upper mantle revives the problem confronted by prior studies of the EPR of explaining a narrow body of partial melt extending tens of kilometers into the mantle [*Wang and Cochran*, 1993; *Magde et al.*, 1995, *Eberle et al.*, 1998]. Higher-resolution seismic studies of the EPR, however, have revealed evidence for partial melt spanning cross-axis widths of only tens of kilometers in the shallowest 50 km of the upper mantle [*Dunn and Forsyth*, 2003] and widths only slightly wider than those simulated in our models (~10 km) just below the crust [*Toomey et al.*, 2007]. These recent findings make such a narrow high melt fraction mantle column beneath the GSC feasible and certainly could be tested using modern seismic techniques.

[39] A possible explanation for a narrow high melt fraction upper mantle that is worthy of further

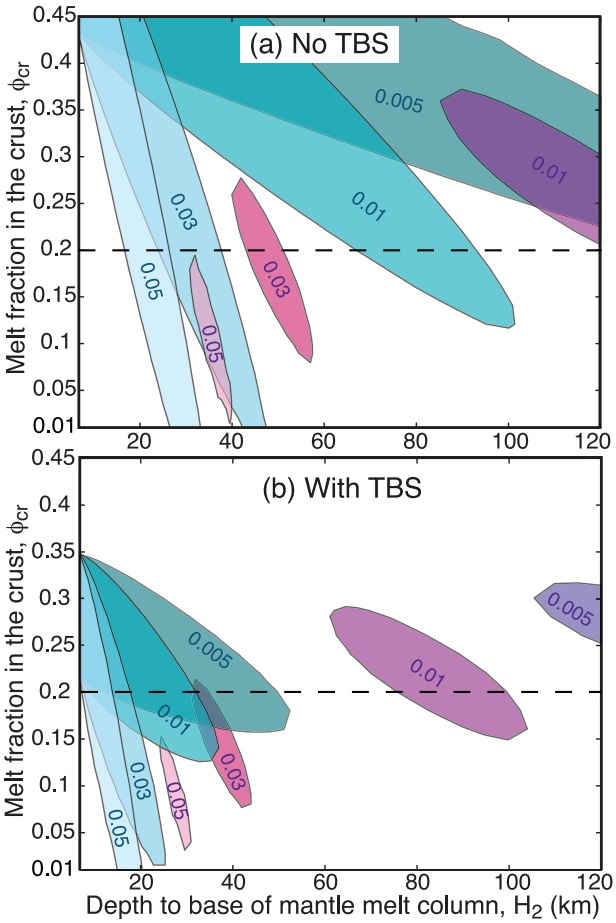

Figure 13. Summary of model results for the case with uniform hydrothermal cooling. (a and b) Minimum average normalized misfit for cases without and with thermal bending stresses. Shaded areas denote values of φ_{cr} and H_2 for which model RMS misfit is $\leq$1.0; numbers within shaded areas denote the value of φ_m. Blue areas correspond to Profile 10 results, and purple-pink areas correspond to Gala3 results. Note that in Figure 13a there is no region for Gala3 with $\varphi_m = 0.005$ because the RMS $\leq$ 1.0 contour did not fall within the range of φ_{cr} and H_2 investigated in the modeling. In Figure 13b the regions for Profile 10 are plotted with minimum RMS $\leq$ 1.1 as there were no model results giving a misfit at or below RMS = 1.0. Axes and dashed reference line are the same as Figure 6.

investigation involves strong buoyant or "dynamic" mantle upwelling [e.g., *Buck and Su*, 1989; *Su and Buck*, 1993; *Turcotte and Phipps Morgan*, 1992; *Spiegelman*, 1993]. If mantle viscosity is sufficiently low and melt retention buoyancy is sufficiently high, the feedback between melt retention and mantle flow tends to focus mantle upwelling in a narrow zone beneath the ridge axis. Such a process could generate the narrow melt column beneath the GSC or other mid-ocean ridges. The dynamics could be more complex when considering the effects of the extraction of water from the mantle to greatly increase its viscosity [*Hirth and Kohlstedt*, 1996]. If these effects are important, then the zone of rapid, narrow upwelling could be below the dry solidus (i.e., below the strong dehydrated layer) [*Choblet and Parmentier*, 2001], with the melt generated from this upwelling zone percolating to shallow depths where it gives rise to axial high topography.

6. Conclusions

[40] The western GSC displays an unusually large axial high that diminishes with distance from the hot spot as magma supply decreases. At the same time, the axial magma lens deepens rapidly away from the hot spot as revealed by multichannel seismic images. This offers the opportunity to test the effects of shallow thermal structure on the origin of the axial high. We explore the cause of the axial high by considering the full range of solutions to a model that simulates the flexure of an accreting lithosphere and the buoyancy of partial melt in the crust and upper mantle [*Shah and Buck*, 2001]. For the Gala3 profile at 92°W where the axial high is especially large the best fitting solutions require at least 3% melt in the upper mantle extending down to depths as great as 45–65 km and 8–20% melt in the crust. Farther to the west in the Profile 10 region at 92.7°W where the axial high is smaller (but still larger and wider than that observed along most of the EPR), the best fitting solutions require at least 1% melt in the upper mantle extending to depths of 65–100 km with 12–20% melt in the crust, or 3% melt in the mantle extending 30–50 km in depth with 1–20% melt in the crust. Solutions in which melt is confined to the crust are less favored because they require an average of >35% partial melt throughout the lower crust, which appears to exceed that allowed by available seismic observations. Our results revive previous suggestions of a narrow (<∼20 km) column of molten material extending well into the upper mantle as contributing to the axial high topography at the GSC and other fast spreading ridges. Such a narrow melt column may have been seismically imaged beneath the East Pacific Rise and suggests that mantle upwelling and melting may be focused beneath the ridge axis due to a buoyant partial melting column. This process may be especially pronounced at the Galapagos Spreading Center due to the influence of the nearby Galapagos hot spot.

Acknowledgments

[41] We thank Dan Scheirer and Ginger Barth at the USGS for constructive presubmission comments. We also thank Suzanne M. Carbotte and Laurent Montesi for their careful and detailed reviews. Ito was supported by grants NSF-OCE-0327051 and NSF-OCE-0351234.

References

Blacic, T. M., G. Ito, J. P. Canales, R. S. Detrick, and J. Sinton (2004), Constructing the crust at the Galápagos Spreading Center 91.3°–95.5°W: Correlation of seismic layer 2A with axial magma lens and topographic characteristics, *J. Geophys. Res.*, *109*, B10310, doi:10.1029/2004JB003066.

Buck, W. R. (2001), Accretional curvature of lithosphere at magmatic spreading centers and the flexural support of axial highs, *J. Geophys. Res.*, *106*, 3953–3960, doi:10.1029/2000JB900360.

Buck, W. R., and W. Su (1989), Focused mantle upwelling below mid-ocean ridges due to feedback between viscosity and melting, *Geophys. Res. Lett.*, *16*, 641–644, doi:10.1029/GL016i007p00641.

Canales, J. P., J. J. Danobeitia, R. S. Detrick, E. E. E. Hooft, R. Bartolome, and D. F. Naar (1997), Variations in axial morphology along the Galápagos spreading center and the influence of the Galápagos hotspot, *J. Geophys. Res.*, *102*, 27,341–27,354, doi:10.1029/97JB01633.

Canales, J. P., G. Ito, R. S. Detrick, and J. Sinton (2002), Crustal thickness along the western Galápagos Spreading Center and the compensation of the Galápagos hotspot swell, *Earth Planet. Sci. Lett.*, *203*, 311–327, doi:10.1016/S0012-821X(02)00843-9.

Canales, J., R. A. Dunn, G. Ito, R. S. Detrick, and J. M. Sinton (2006), Investigating the role of magma supply on crustal accretion processes; seismic structure and axial morphology of the western Galapagos spreading center, *Eos Trans. AGU*, *87*, Fall Meet. Suppl., Abstract V14A–04.

Carbotte, S. M., A. Solomon, and G. Ponce-Correa (2000), Evaluation of morphological indicators of magma supply and segmentation from a seismic reflection study of the East Pacific Rise 15°30′–17°N, *J. Geophys. Res.*, *105*, 2737–2759, doi:10.1029/1999JB900245.

Chen, Y. J., and J. Lin (2004), High sensitivity of ocean ridge thermal structure to changes in magma supply: The Galapagos Spreading Center, *Earth Planet. Sci. Lett.*, *221*, 263–273, doi:10.1016/S0012-821X(04)00099-8.

Chen, Y. J., and W. J. Morgan (1990), Rift valley/no rift valley transition at mid-ocean ridges, *J. Geophys. Res.*, *95*, 17,571–17,581.

Choblet, G., and E. M. Parmentier (2001), Mantle upwelling and melting beneath slow spreading centers: Effects of variable rheology and melt productivity, *Earth Planet. Sci. Lett.*, *184*, 589–604, doi:10.1016/S0012-821X(00)00330-7.

Cochran, J. R. (1979), Analysis of isostasy in the world ocean, *J. Geophys. Res.*, *84*, 4713–4729, doi:10.1029/JB084iB09p04713.

Collier, J. S., and M. C. Sinha (1992), Seismic mapping of a magma chamber beneath the Valu Fa Ridge, Lau Basin, *J. Geophys. Res.*, *97*, 14,031–14,053, doi:10.1029/91JB02751.

Crawford, W. C., S. C. Webb, and J. A. Hildebrand (1999), Constraints on melt in the lower crust and Moho at the East Pacific Rise, 9°48′N, using seafloor compliance measurements, *J. Geophys. Res.*, *104*, 2923–2939, doi:10.1029/1998JB900087.

Cushman, B., J. Sinton, G. Ito, and J. E. Dixon (2004), Glass compositions, plume-ridge interaction, and hydrous melting along the Galápagos spreading center, 90.5°W to 98°W, *Geochem. Geophys. Geosyst.*, *5*, Q08E17, doi:10.1029/2004GC000709.

Detrick, R. S., A. J. Harding, G. M. Kent, J. A. Orcutt, J. Mutter, J. Orcutt, and P. Buhl (1993), Seismic structure of the southern East Pacific Rise, *Science*, *259*, 499–503, doi:10.1126/science.259.5094.499.

Detrick, R. S., J. M. Sinton, G. Ito, J. P. Canales, M. Behn, T. Blacic, B. Cushman, J. E. Dixon, D. W. Graham, and J. J. Mahoney (2002), Correlated geophysical, geochemical, and volcanological manifestations of plume-ridge interaction along the Galápagos Spreading Center, *Geochem. Geophys. Geosyst.*, *3*(10), 8501, doi:10.1029/2002GC000350.

Dunn, R. A., and D. W. Forsyth (2003), Imaging the transition between the region of mantle melt generation and the crustal magma chamber beneath the southern East Pacific Rise with short-period Love waves, *J. Geophys. Res.*, *108*(B7), 2352, doi:10.1029/2002JB002217.

Dunn, R. A., D. R. Toomey, and S. C. Solomon (2000), Three-dimensional seismic structure and physical properties of the crust and shallow mantle beneath the East Pacific Rise at 9°30′N, *J. Geophys. Res.*, *105*, 23,537–23,555, doi:10.1029/2000JB900210.

Dunn, R. A., V. Lekic, R. S. Detrick, and D. R. Toomey (2005), Three-dimensional seismic structure of the Mid-Atlantic Ridge (35°N): Evidence for focused melt supply and lower crustal dike injection, *J. Geophys. Res.*, *110*, B09101, doi:10.1029/2004JB003473.

Eberle, M. A., and D. W. Forsyth (1998), An alternative, dynamic model of the axial topographic high at fast spreading ridges, *J. Geophys. Res.*, *103*, 12,309–12,320, doi:10.1029/98JB00437.

Eberle, M. A., D. W. Forsyth, and E. M. Parmentier (1998), Constraints on a buoyant model for the formation of the axial topographic high on the East Pacific rise, *J. Geophys. Res.*, *103*, 12,291–12,307, doi:10.1029/98JB00030.

Garrido, C. J., P. B. Kelemen, and G. Hirth (2001), Variation of cooling rate with depth in lower crust formed at an oceanic spreading ridge: Plagioclase crystal size distributions in gabbros from the Oman ophiolite, *Geochem. Geophys. Geosyst.*, *2*(10), 1041, doi:10.1029/2000GC000136.

Henstock, T. J., A. W. Woods, and R. S. White (1993), The accretion of oceanic crust by episodic sill intrusion, *J. Geophys. Res.*, *98*, 4143–4161, doi:10.1029/92JB02661.

Hirth, G., and D. L. Kohlstedt (1996), Water in the oceanic upper mantle: Implications for rheology, melt extraction, and the evolution of the lithosphere, *Earth Planet Sci. Lett.*, *144*, 93–108.

Hooft, E. E., and R. S. Detrick (1995), Relationship between axial morphology, crustal thickness, and mantle temperature along the Juan de Fuca and Gorda Ridges, *J. Geophys. Res.*, *100*, 22,499–22,508, doi:10.1029/95JB02502.

Hooft, E. E., R. S. Detrick, and G. M. Kent (1997), Seismic structure and indicators of magma budget along the southern East Pacific Rise, *J. Geophys. Res.*, *102*, 27,319–27,340, doi:10.1029/97JB02349.

Ito, G., and M. D. Behn (2008), Magmatic and tectonic extension at mid-ocean ridges: 2. Origin of axial morphology, *Geochem. Geophys. Geosyst.*, *9*, Q09012, doi:10.1029/2008GC001970.

Kent, G. M., A. J. Harding, and J. A. Orcutt (1993a), Distribution of magma beneath the East Pacific Rise near the 9°03′N overlapping spreading center from forward modeling of common depth point data, *J. Geophys. Res.*, *98*, 13,971–13,995, doi:10.1029/93JB00706.

Kent, G. M., A. J. Harding, and J. A. Orcutt (1993b), Distribution of magma beneath the East Pacific Rise between the Clipperton Transform and the 9°17′N deval from forward modeling of common depth point data, *J. Geophys. Res.*, *98*, 13,945–13,969, doi:10.1029/93JB00705.

Kuo, B. Y., D. W. Forsyth, and E. M. Parmentier (1986), Flexure and thickening of the lithosphere at the East Pacific Rise, *Geophys. Res. Lett.*, *13*, 681–684, doi:10.1029/GL013i007p00681.

Madsen, J. A., D. W. Forsyth, and R. S. Detrick (1984), A new isostatic model for the East Pacific Rise crest, *J. Geophys. Res.*, *89*, 9997–10015, doi:10.1029/JB089iB12p09997.

Madsen, J. A., R. S. Detrick, J. C. Mutter, P. Buhl, and J. A. Orcutt (1990), A two- and three-dimensional analysis of gravity anomalies associated with the East Pacific Rise at 9°N and 13°N, *J. Geophys. Res.*, *95*(B4), 4967–4987, doi:10.1029/JB095iB04p04967.

Magde, L. S., R. S. Detrick, and the TERA Group (1995), Crustal and upper mantle contribution to the axial gravity anomaly at the southern East Pacific Rise, *J. Geophys. Res.*, *100*, 3747–3766, doi:10.1029/94JB02869.

McNutt, M. (1979), Compensation of oceanic topography, an application of the response function technique to the Surveyor area, *J. Geophys. Res.*, *84*, 7589–7598.

Parker, R. L. (1973), The rapid calculation of potential anomalies, *J. R. Astron. Soc.*, *31*(4), 447–455.

Parmentier, E. M., and W. F. Haxby (1986), Thermal stresses in the oceanic lithosphere: Evidence from geoid anomalies at fracture zones, *J. Geophys. Res.*, *91*(B7), 7193–7204, doi:10.1029/JB091iB07p07193.

Parsons, B., and J. G. Sclater (1977), An analysis of the thermal structure of the plates, *J. Geophys. Res.*, *82*, 803–827, doi:10.1029/JB082i005p00803.

Phipps Morgan, J., and Y. J. Chen (1993), Dependence of ridge-axis morphology on magma supply and spreading rate, *Nature*, *364*, 706–708, doi:10.1038/364706a0.

Sandwell, D. T., and W. H. F. Smith (1997), Marine gravity anomaly from Geosat and ERS1 satellite altimetry, *J. Geophys. Res.*, *102*, 10,039–10,054, doi:10.1029/96JB03223.

Scheirer, D. S., and K. C. Macdonald (1993), Variation in cross-sectional area of the axial ridge along the East Pacific Rise: Evidence for the magmatic budget of a fast spreading center, *J. Geophys. Res.*, *98*, 7871–7885, doi:10.1029/93JB00015.

Scheirer, D. S., D. W. Forsyth, M. H. Cormier, and K. C. Macdonald (1998), Shipboard geophysical indications of asymmetry and melt production beneath the East Pacific Rise near the MELT experiment, *Science*, *280*, 1221–1223, doi:10.1126/science.280.5367.1221.

Searle, R. C., and A. S. Laughton (1981), Fine-scale sonar study of tectonics and volcanism on the Reykjanes Ridge, report, pp. 5–13, Inst. of Oceanogr. Sci., Leeds, UK.

Sempéré, J. M., J. Palmer, D. Christie, J. Phipps Morgan, and A. Shor (1991), Australian-Antarctic Discordance, *Geology*, *19*, 429–432, doi:10.1130/0091-7613(1991)019<0429:AAD>2.3.CO;2.

Shah, A. K., and W. R. Buck (2001), Causes for axial high topography at mid-ocean ridges and the role of crustal thermal structure, *J. Geophys. Res.*, *106*, 30,865–30,879, doi:10.1029/2000JB000079.

Shah, A. K., and W. R. Buck (2003), Plate bending stresses at axial highs, and implications for faulting behavior, *Earth Planet. Sci. Lett.*, *211*, 343–356, doi:10.1016/S0012-821X(03)00187-0.

Shah, A. K., and W. R. Buck (2006), The rise and fall of axial highs during ridge jumps, *J. Geophys. Res.*, *111*, B08101, doi:10.1029/2005JB003657.

Sinton, J., R. Detrick, J. P. Canales, G. Ito, and M. Behn (2003), Morphology and segmentation of the Western Galápagos spreading center, 90.5°–98°W: Plume-ridge interactions at an intermediate spreading ridge, *Geochem. Geophys. Geosyst.*, *4*(12), 8515, doi:10.1029/2003GC000609.

Spiegelman, M. (1993), Physics of melt extraction: Theory, implications and applications, *Philos. Trans. R. Soc. London Ser. A*, *342*, 23–41, doi:10.1098/rsta.1993.0002.

Su, W., and W. R. Buck (1993), Buoyancy effects on mantle flow under mid-ocean ridges, *J. Geophys. Res.*, *98*, 12,191–12,205, doi:10.1029/93JB00994.

Talwani, M., J. L. Wrzel, and M. Landisman (1959), Rapid gravity computations for two-dimensional bodies with application to the Mendocino submarine fracture zone, *J. Geophys. Res.*, *64*, 49–59, doi:10.1029/JZ064i001p00049.

Tolstoy, M., A. J. Harding, and J. A. Orcutt (1997), Deepening of the axial magma chamber on the southern East Pacific Rise toward the Garrett Fracture Zone, *J. Geophys. Res.*, *102*, 3097–3108, doi:10.1029/96JB03226.

Toomey, D. R., S. C. Solomon, and G. M. Purdy (1994), Tomographic imaging of the shallow crustal structure of the East Pacific Rise at 9°30′N, *J. Geophys. Res.*, *99*, 24,135–24,157, doi:10.1029/94JB01942.

Toomey, D. R., D. Jousselin, R. A. Dunn, W. S. D. Wilcock, and R. S. Detrick (2007), Skew of mantle upwelling beneath the East Pacific Rise governs segmentation, *Nature*, *446*, 409–414, doi:10.1038/nature05679.

Turcotte, D. L., and J. Phipps Morgan (1992), The physics of magma migration and mantle flow beneath a mid-ocean ridge, in *Mantle Flow and Melt Generation Beneath Mid-Ocean Ridges*, *Geophys. Monogr. Ser.*, vol. 71, edited by J. Phipps Morgan et al., pp. 155–182, AGU, Washington, D. C.

Turcotte, D. L., and G. Schubert (1982), *Geodynamics: Applications of Continuum Physics to Geological Problems*, 450 pp., John Wiley, New York.

Vera, E. E., J. C. Mutter, P. Buhl, J. A. Orcutt, A. J. Harding, M. E. Kappus, R. S. Detrick, and T. M. Brocher (1990), The structure of 0- to 0.2-m.y.-old oceanic crust at 9°N on the East Pacific Rise from expanding spread profiles, *J. Geophys. Res.*, *95*, 15,529–15,556, doi:10.1029/JB095iB10p15529.

Wang, X., and J. R. Cochran (1993), Gravity anomalies, isostasy, and mantle flow at the East Pacific Rise crest, *J. Geophys. Res.*, *98*, 19,505–19,531, doi:10.1029/93JB01551.

White, W. M., A. R. McBirney, and R. A. Duncan (1993), Petrology and geochemistry of the Galápagos Islands: Portrait of a pathological mantle plume, *J. Geophys. Res.*, *98*, 19,533–19,563, doi:10.1029/93JB02018.

Wilson, D. S. (1992), Focused mantle upwelling beneath mid-ocean ridges: Evidence from seamount formation and isostatic compensation of topography, *Earth Planet. Sci. Lett.*, *113*, 41–55, doi:10.1016/0012-821X(92)90210-M.